TESI DI DOTTORATO

UNIVERSITA' DEGLI STUDI DI NAPOLI FEDERICO II

DIPARTIMENTO DI INGEGNERIA BIOMEDICA, ELETTRONICA
E DELLE TELECOMUNICAZIONI

DOTTORATO DI RICERCA IN
INGEGNERIA ELETTRONICA E DELLE TELECOMUNICAZIONI

Electromagnetic Modeling and Information Extraction from SAR Data

GERARDO DI MARTINO

Il Coordinatore del Corso
Ch.mo Prof. Giovanni Poggi

Il Tutore
Ch.mo Prof. Daniele Riccio

Anno accademico 2007–2008

Index

Introduction **5**

Chapter 1 SAR: direct models and information mining 7
1.1 SAR fundamentals
1.1.1 SAR raw data processing
1.2 Information extraction from SAR data
1.2.1 Model-based information extraction
1.3 SAR raw signal simulation
1.4 The new challenge of high resolution
1.4.1 Analysis of actual TerraSAR-X data

References

Chapter 2 Direct modeling of natural surfaces 23
2.1 Fractal models
2.1.1 Fractal description of natural surfaces
2.1.1.1 Fractional Brownian motion process
2.1.1.2 Weierstrass-Mandelbrot function
2.1.1.3 Connection between fBm and WM surfaces
2.1.2 Scattering from fractional Brownian surfaces
2.1.2.1 Physical-optics solution
2.1.2.2 Small Perturbation Method
2.2 The ocean surface
2.2.1 Fully developed sea surface spectrum
2.2.2 Bragg scattering
2.2.3 Effects of oil pollutants on sea surface

References

Chapter 3 SAR simulation tools 43
3.1 A fractal simulation and analysis chain
3.1.1 Fractal framework assessment
3.1.2 Case studies

3.1.2.1 Comparison with actual data
3.1.2.2 Flooding
3.1.2.3 Volcano eruption
3.2 Simulation of ocean scenes covered by oil slicks
3.2.1 Generation of oil slicks with arbitrary shapes
3.2.2 Image analysis
3.2.2.1 Fractal technique
3.2.2.2 Radiometric techniques

References

Chapter 4 Microwave imaging 73
4.1 Imaging of one-dimensional fractal profiles
4.1.1 Pentland model
4.1.2 The small slope analytical model
4.1.2.1 Fractional Gaussian noise (fGn)
4.1.2.2 The imaging model
4.1.2.3 The numerical framework
4.1.2.4 The obtained results
4.1.3 The developed software
4.1.4 Simulation results
4.2 The two-dimensional problem: preliminary results

References

Summary and conclusions 101

Introduction

The key goal of this thesis work lies in the development of models and tools in support of value-added information extraction from Synthetic Aperture Radar amplitude-only images.

In the last decades earth observation instruments provided a great amount of images relevant to any part of the world. These data could be potentially helpful for a wide range of human activities, ranging from agriculture to rural and urban planning and disaster monitoring and assessment. However, practical use of these data is often limited by the lack of efficient, possibly unsupervised, tools for the retrieving of effective information.

In this thesis the first steps toward a modeling of the whole imaging process is provided. In particular, we discuss in detail the fundamentals of the Synthetic Aperture Radar in its standard and well known working configuration, highlighting the need for an adequate modeling able to guarantee effective high resolution data description (Chapter 1). In fact, the statistics of this kind of images are often very different from those used in the modeling of low resolution data. First results coming from the analysis of the first TerraSAR-X high resolution data are presented here and represent the first original contribution of this thesis.

In Chapter 1 not only the working geometries and SAR performances are presented but also a conceptual scheme for the simulation of the primary signal collected by the sensor called *raw data*. Simulators, in fact, are important tools supporting the design and project of new sensors and are able to conveniently lead the criterions for setting the mission parameters as they take into accounts the applications they are planned for. Furthermore, they can be used to conveniently address the inverse problem starting from the complete solution of the direct one.

In fact, the development of effective information extraction techniques from SAR data and the synthesis of automatic tools for image analysis mandatory pass through the development of adequate direct models relating the image to the parameters of the surface. Thus, the direct models can become the starting point toward the availability of inversion techniques and physically-based classification

techniques. The models used in this thesis work are detailed in Chapter 2. In particular, the geometric and electromagnetic models for natural surfaces are presented, both for natural terrain and for the ocean sea surface.

After having introduced the different techniques to collect and model SAR data, we move to discuss the possibility of retrieving information analyzing those data.

In particular, in Chapter 3 we present a fractal framework for the simulation of SAR images relevant to simulated disaster scenarios. Such an instrument can be used to increase the understanding of the physical mechanisms underlying radar image formation in case of disasters. In, fact, the main problem of the scientist working on the development of remote sensing techniques for disaster monitoring is the lack or the limitedness of an accurate ground truth. The proposed simulator makes possible to perform parametric studies on canonical disasters scenarios with a perfectly known ground truth. Furthermore, it can be used to obtain images relevant to both pre- and post-crisis situations, providing the possibility to develop a test bed of simulated images to be used for the testing of change detection techniques. Relevant case studies are presented with regard to different kinds of natural disasters. Finally, a novel change detection technique based on the estimation of significant parameters and supported by fractal concepts is described. Results on the simulation of images relevant to ocean scenes covered with oil slicks of arbitrary shape are also presented.

In Chapter 4 we cope with the problem of radar imaging of fractal surfaces. In particular, we develop a rigorous analytical formulation for the problem in case a small slope regime can be assumed for the profile. The proposed model allows for the computation of the structure function and of the power density spectrum of the image in closed form. The proposed model is validated through an appropriate numerical framework base on the sound physical models presented in Chapter 2. The first steps toward the extension to the two-dimensional case are also provided. Note that the development of this kind of direct modeling is of key importance for every image analysis technique based on the evaluation of global statistics on SAR images.

Chapter 1

SAR: Direct Modeling and Information Mining

In the last decades earth observation instruments provided a great amount of images relevant to any part of the world. These data could be potentially helpful for a wide range of human activities, ranging from agriculture to rural and urban planning and disaster monitoring and assessment. While information extraction from optical data can be often performed via empiric techniques, due to the similarity of these images with those perceived from the human eyes, microwave data need to be treated differently and their interpretation is absolutely not trivial.

Hereafter we focus on Synthetic Aperture Radar (SAR) images of the earth surface, which present all the advantages of microwave imaging, in particular the all-weather, all-time capabilities and a huge increase in resolution with respect to the Real Aperture Radar (RAR). However, their interpretation is not straightforward: in part because of the *speckle*, the multiplicative noise affecting these images, which is responsible for their well-known *salt and pepper* behavior; moreover, the relation occurring between the physical parameters of the observed scene and the characteristics of the image is often involved or, at least, is very different with respect to the case of optical imaging. This is the reason why the analysis of radar images can't be carried on via empirical techniques, but needs to be based on sound physical models: an accurate modeling of the imaging process represents the main road toward an effective retrieving of value-added information from the data.

In this scenario simulation tools can be of great relevance in the understanding of SAR signal formation and in the development of inverse methods for the estimation of significant geophysical parameters from the image.

In this chapter the fundamentals of SAR sensor and of the standard processing of raw data are described. However, special attention is paid to the rationale of information extraction based on direct modeling and on the simulation of SAR raw signal. Finally, the first results obtained from the analysis of high resolution TerraSAR-X images are reported. They clearly highlight the dependence of the models also on sensor parameters such as geometric resolution.

1.1 SAR fundamentals

The SAR system can work in accord to different operational modes of acquisition: in this section we focus on the stripmap configuration, in which the antenna points along a fixed direction with respect to the platform flight path and its footprint defines an illuminated strip on the observed surface as the sensor moves [1].

The SAR raw signal can be evaluated as the superposition of the elementary returns from the illuminated surface weighted via its reflectivity function $\gamma(x,r)$:

$$h(x',r') = \iint dxdr\,\gamma(x,r)\,g(x'-x,r'-r;r) \tag{1.1}$$

and the unit impulse response of the SAR system $g(\cdot)$, in the case of a stripmap acquisition mode and of a transmitted chirped pulse, can be expressed as:

$$\begin{aligned} g(x'-x,\quad r'-r;\quad r) &= \exp\left[-j\frac{4\pi}{\lambda}\Delta R\right]\cdot \\ \exp\left[-j\frac{4\pi}{\lambda}\frac{\Delta f/f}{c\tau}(r'-r-\Delta R)^2\right]&\cdot w^2\left(\frac{x'-x}{X}\right)\mathrm{rect}\left[\frac{(r'-r-\Delta R)}{c\tau/2}\right] \end{aligned} \tag{1.2}$$

where, referring to Fig. 1:

- P is the generic scattering point on the observed surface and its coordinates (x,r,ϑ) are given in a cylindrical reference system for which the azimuth direction coincides with the sensor flight path; $\vartheta(x,r)$ is the local incidence angle, which depends on the

local geometry of the surface; R is the antenna-to-target distance and $\Delta R=R-r$;

- c is the speed of light, f and λ are respectively the carrier frequency and the corresponding wavelength, Δf is the chirp bandwidth and τ its duration time;
- $w(\cdot)$ is the antenna illumination function, $X=\lambda R_0/L_x$ is the real antenna azimuth footprint (we assume that $w(\cdot)$ is negligible when the absolute value of its argument is larger than 1/2, and that it is an even function), where L_x is the azimuth dimension of the real antenna and R_0 is the distance from the line of flight to the centre of the scene.

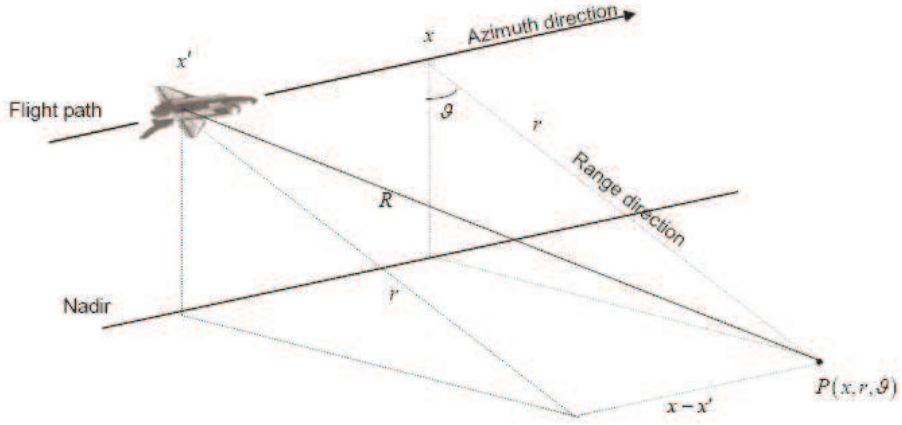

Figure 1 Geometry of the problem.

Starting from Eq. (1.2) we can evaluate the *Transfer Function* (TF) of the SAR system. In particular, the Fourier Transform (FT) of (1.2) can be expressed as [1]:

$$H(\xi,\eta)=\iint \gamma(x,r)G(\xi,\eta;r)\exp[-j\xi x]\exp[-j\eta r]dxdr \qquad (1.3)$$

where $G(\cdot)$ is the TF of the SAR system in the stripmap acquisition mode, given by the following FT:

$$G(\xi,\eta;r)=\iint g(x-x',r-r';r)\exp\left[-j\xi(x'-x)\right]\exp\left[-j\eta(r'-r)\right]dx'dr' \tag{1.4}$$

Let us note that, when the *r*-dependence in Eq. (1.4) can be neglected, Eq. (1.1) becomes a two-dimensional convolution, leading to the following simplified expression for Eq. (1.3):

$$H(\xi,\eta)=\iint \gamma(x,r)\exp(-j\xi x)\exp(-i\eta r)G(\xi,\eta)dxdr=\Gamma(\xi,\eta)G(\xi,\eta) \tag{1.5}$$

In general the TF in (1.4) can be expressed as follows:

$$G(\xi,\eta;r)=\exp\left[j\frac{\eta^2}{4b}\right]\exp\left[j\frac{\xi^2(r/R_0)}{4a\left(1+\eta\lambda/(4\pi)\right)}\right]rect\left[\frac{\eta}{2bc\tau/2}\right]w^2\left(\frac{\xi}{2aX}\right) \tag{1.6}$$

where

$$a=\frac{2\pi}{\lambda R_0} \tag{1.7}$$

$$b=\frac{4\pi(\Delta f/f)}{\lambda c\tau} \tag{1.8}$$

1.1.1 SAR raw data processing

The obtained raw signal needs to be elaborated in order to provide the final SAR image [1]. The main goal of the SAR processor is to adequately combine all the received backscattered contributions, which in the raw signal are spread out over all the extension [X,$c\tau/2$], to achieve the best resolution.

The standard SAR processing, in the hypothesis that the *r*-dependence in Eq. (1.4) can be neglected, consists in a de-convolution applied to $h(x',r')$ to compensate for the convolution factor $g(x',r',r_0)$ and obtain an estimation of the reflectivity function. This operation

can be efficiently implemented in the Fourier domain through a simple multiplication:

$$\hat{\Gamma}(\xi,\eta) = \Gamma(\xi,\eta) \cdot G(\xi,\eta) \cdot G^{*}(\xi,\eta) \tag{1.9}$$

where * stands for the conjugation operator. Combining Eq. (1.9) with Eq. (1.6) in case of a space-invariant processing we obtain:

$$\hat{\gamma}(x',r') = \iint \gamma(x,r) \exp\left(-j\frac{4\pi}{\lambda}r\right) \operatorname{sinc}\left[\frac{\pi}{\Delta x}(x'-x)\right] \operatorname{sinc}\left[\frac{\pi}{\Delta r}(r'-r)\right] dx dr \tag{1.10}$$

where Δx and Δr are the geometrical resolution of the final image in azimuth – slant range, respectively, and are equal to:

$$\Delta x = \frac{L}{2} \tag{1.11}$$

$$\Delta r = \frac{c}{2\Delta f} \tag{1.12}$$

Accordingly, the SAR image can be seen as a convolution between the reflectivity function and two sinc functions, one in the azimuth and one in the range direction, whose main lobes present a -3dB width equal to the geometric resolutions of the sensor as defined in Eq. (1.11) and Eq. (1.12), respectively. Let us note that this elaboration is easily performed in the Fourier domain: in fact, the availability of efficient FFT codes determines a strong decrease in the computational complexity with respect to the required convolution in the spatial domain.

This kind of space-invariant processing is called *narrow focusing* and as a result only the centre of the scene is perfectly focused. To achieve optimum focusing (*wide focusing*) in the general space-variant case the FT of the reflectivity function requires to be computed on a deformed grid. Efficient processing codes in the Fourier domain have been developed to assure wide focusing of the data, but providing the

details of these algorithms is beyond the scope of this thesis work for detailed information see Ref. [1]). For our purposes the key result is the one presented in Eq. (1.10) which clearly shows how the SAR image is essentially equal to a sinc-convolved version of the reflectivity.

Now that the fundamentals of SAR remote sensing are assessed, in the next section we will investigate why and how direct models can support information mining from this kind of microwave images.

1.2 Information extraction from SAR data

Remote sensing sensors provide a great amount of data relevant to any part of the world. In particular, SAR sensors are able to image the surface of the earth in practically any weather and illumination condition. Furthermore, in the last years, high-resolution sensor made possible the analysis of radar images with sub-metric resolutions.

However, practical use of SAR data is still very limited by the lack of efficient, possibly unsupervised, tools for the retrieving of effective information to be used in a great variety of applications. Several approaches devoted to define instruments and tools for data interpretation were presented in literature, showing, at least in principle, the potentiality of satellite and aerial technique as a support in agriculture, urban planning, monitoring and eventually prevention, of natural (flooding, volcanic risk, landslides, etc.) and human-made disasters (oil spills, fires, etc.). Most of these approaches are based on empirical analyses of remotely sensing data, essentially driven by user needs. These analyses are generally supervised; and, to be effective, it is often required that the supervisor holds a remarkable level of competence with reference both to the sensors, and to the image formation mechanisms.

Furthermore, being the SAR data strongly dependent on the physical parameters of the observed surface, the retrieving of significant parameters such as water content of the soil, electromagnetic parameters, etc. would be possible, at least in principle. In fact, the effectiveness of the retrieving is strongly dependent on the availability of adequate models for the phenomena under investigation.

Among remote sensing sensors, the imaging ones take the advantage of generating synoptic views of the area under observation; in this case, the rationale for the feature identification techniques is usually based on the concepts of image texture analysis. Textures on remotely sensed images are related to morphological and geological features, land use and social organization of the observed scene. All the image processing techniques used to segment and classify radar data are based on statistical models, which require particular assumptions on the imaged surface (a review of great part of these models can be found in Ref. [2]). In this sense the use of a particular stochastic model should be driven by an a priori knowledge of some properties of the surface. Moreover, also the sensor parameters can affect the choice of the above-mentioned models: as an example, in the following we investigate the dependence of data statistics on sensor resolution. In fact, we find out that the stochastic model used in the analysis of low resolution data cannot be simply exported to high resolution scenarios.

These remarks point out to the core of the problem faced in this thesis work. In fact, the development of effective information extraction techniques from SAR data and the synthesis of automatic tools for image analysis pass through the development of adequate direct models relating parameters of the image to those of the surface. Thus, the direct models can become the starting point toward the development of inversion techniques and physically-based classification algorithms.

Let us try to understand better what kind of models are required to obtain this goal.

1.2.1 Model-based information extraction

The first model we need is a geometrical model for the observed surface. In this thesis we are interested in natural surfaces: the better way to model this class of surfaces is to consider them just as one realization of a stochastic process. In fact, natural surfaces are the result of the combination of different geophysical mechanisms (erosions, tectonic movements, etc.) mixing in a random way. This is the reason why we are interested more in global statistics of their radar images then in punctual, deterministic aspects. Conversely, in case an

urban area is of interest we would like to retrieve some deterministic information (on building heights, streets widths, etc.): this requires a different kind of model for the surface, a deterministic, punctual one.

The parameters used for the geometrical description of the surface are those we would like to retrieve from the image. Thus, for inversion purposes a sound modeling of surface geometry is of key importance. Unfortunately, the relation occurring between the surface and its image is strongly non-linear and this makes the extraction procedure not straightforward.

Once we have described the surface we need to model the interaction between the surface and the electromagnetic field impinging on it. Several scattering models are available in the literature; some are heuristics while others are analytical and physically-based. For our purposes, we are interested in the analytical ones that are able to keep trace of the parameters used for the geometrical description of the surface. Hence, we need scattering analytical models, which are able to accept as input those particular parameters. In fact, obviously, each surface calls for an appropriate electromagnetic modeling: the use of a model not specifically tailored to the surface can lead to huge errors in the evaluation of the backscattered signal.

Combining the geometrical and the electromagnetic models leads to the evaluation of the mean square value of the received signal. However, radar images are affected by *speckle* noise resulting from the coherent character of the imaging system. In particular, it is due to the fact that the resolution cell is great with respect to the wavelength of the impinging field, thus containing a set of interfering scatterers. Speckle provides SAR images with their characteristic *salt and pepper* appearance. To adequately treat this phenomenon we need also a statistical model for these random signal fluctuations. As for the scattering model, also the speckle seems to be dependent on the characteristics of the surface.

Once we have these three models we can begin to develop adequate model-based inversion techniques to retrieve the parameters of interest of the surface. These models are also the core of the SAR raw signal simulator presented in Ref. [3]. Such a powerful instrument can be used both to validate the models and to provide a set of simulated SAR images to be used as a test bed for the development of

information extraction techniques (see Chapter 3). In the following section the rationale of the simulation procedure is provided.

1.3 SAR raw signal simulation

Within the framework of SAR studies, it is convenient to simulate the received signal before any processing (with the exception of the heterodyne down-converter). This is the signal we called *raw* in the first section.

As already said, simulation of canonical scenarios may simplify experimentation of processing algorithms, as well as development of pattern recognition and feature extraction techniques. Simulation may play a significant role in studies concerning *speckle* noise and may contribute toward optimizing SAR system parameters.

A simulation code must meet a number of stringent constraints. The scenario to be simulated should be rather general and possibly time varying, either deterministically or stochastically. As we have seen in the previous section, it should rely upon sound direct models both from the geometrical and for the electromagnetic point of view. Since we are interested in simulating extended scenes we need a macroscopic description of the altitude profile at scales comparable to the system resolution, since the microscopic profile is characterized statistically according to the geometrical model of the surface. Last, but not least, the numerical code should be efficient, fast and (computer) memory saving. These features are usually in competition, and the ultimate solution generally comes to be an engineering compromise.

The rationale of the simulation is shown in Fig. 2. It is possible to note that the upper part, the one named SAR Acquisition, implements the simulation of the SAR raw signal and it is composed by the following blocks: the scattering block, which requires as inputs the geometrical and electromagnetic description of the surface; the geometrical distortions block, which takes into account for the azimuth – slant-range geometry of the acquisition system and, finally, there is the block devoted to the convolution with the SAR transfer function. In the lower part of Fig. 2, the SAR processing chain is presented, where the SAR focused image is indicated as a product of

Level 1a and a product of Level 2 is the final target of information extraction techniques.

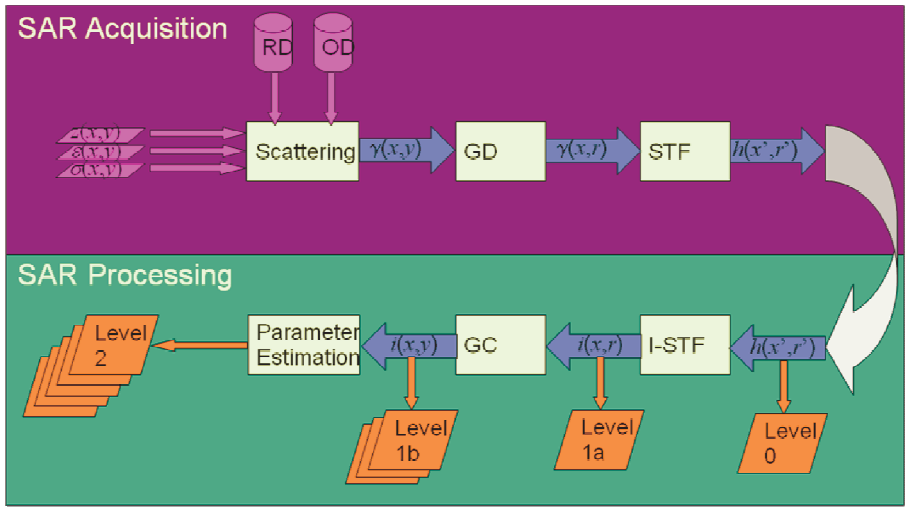

Figure 2 Rationale of SAR acquisition and data processing.

An example of efficient SAR raw signal simulator for the stripmap acquisition mode is given in Ref. [3]. This simulator has been the key instrument for the development of the models, tools and techniques presented in Chapter 3.

1.4 The new challenge of high resolution

As we already mentioned, the new generation of high resolution SAR sensors is providing a huge amount of data with meter and sub-meter resolutions. However, it is no longer possible to cope with this increase in resolution with the use of old models, tailored to low resolution data and sensors. The best example is provided by the modeling of speckle noise. Hereafter, the first steps towards new models tailored to high resolution imaging are briefly reported. The goal of this section is to highlight the need for new physically-based models; hence an accurate description of the speckle is beyond the scope of this work. Anyway, extended references are reported at the end of the chapter on this subject.

For low resolution sensors speckle noise was generally studied in the framework of the so called fully developed speckle. To make this assumption several hypothesis have to hold allowing the use of the central limit theorem to obtain a Rayleigh-distributed amplitude image over homogeneous zones. One of these hypotheses is strictly related to the resolution of the sensor: in particular, the dimension of the resolution cell should be very great with respect to the wavelength of the incident field. This was the case for low resolution sensors, as ERS or Envisat missions, but it can be no longer true for high resolution ones.

Note that the great majority of semi-automatic classification techniques applied on SAR images are based on the hypothesis of a Rayleigh distribution for the amplitude image: falling this hypothesis the elaboration results can be very inaccurate [2]. Hence, the importance of the knowledge of adequate speckle noise statistics is evident. In the following the first results of the statistical analysis of actual TerraSAR-X images are presented to support the idea that with the coming of high resolution SAR sensors microwave remote sensing is entering a completely different scenario, calling for its own models and tools.

1.4.1 Analysis of actual TerraSAR-X data

In this section a comparison between the statistics of low resolution and high resolution data is provided. This comparison is carried out through the estimation of the Normalized Moments (NM) of the intensity I of homogeneous patches of the considered images. The NM are defined as follows:

$$NM_n = \frac{\mathrm{E}(I^n)}{\left[\mathrm{E}(I)\right]^n}. \tag{1.13}$$

The NM in the case of fully developed speckle [4] present a known behavior: in fact, if the amplitude of the image can be modeled as Rayleigh-distributed, its intensity will follow a negative exponential distribution. The NM of this distribution are equal to $n!$, where n is the order of the considered moment. This behavior can be

used to determine whether or not the statistics of the data are in accordance with the fully developed speckle model [5].

Another distribution frequently invoked to model the speckle in some specific situations is the K-distribution [6]-[8]. It has been successfully used to describe sea clutter: in fact, for the sea surface the fully developed speckle hypothesis of not-correlated scatterers within a resolution cell is certainly not satisfied, given the periodic character of this kind of surface. The effect of the failure of this particular hypothesis is a decrease in the number of effective scatterers inside a resolution cell: this effect is someway similar to the one obtained through a decrease in the resolution cell dimensions. For this reason here we use the K-distribution to fit the behavior of the NM of high resolution data. In fact, the NM relevant to a K-distributed noise on an homogeneous area are known and are given by the following expression [6]:

$$NM_n = \frac{\Gamma(n+\alpha)n!}{\Gamma(\alpha)\alpha^n} \tag{1.14}$$

$$\alpha = N(1+\nu), \tag{1.15}$$

where N is the number of scatterers within the resolution cell and $\nu > -1$ is a parameter of the K-distribution. The parameter α can be easily estimated from the data evaluating their second order moment.

The area chosen for this experiment is located close to Agrigento, Italy: in fact, one low resolution ERS image (20 x 20 m^2 pixel spacing) and one high resolution spotlight TerraSAR one (1.1 x 1.6 m^2 pixel spacing) are available for this zone. A subset of both images approximately relevant to the same portion of surface and fulfilling the necessary criterion of homogeneity was selected. Obviously, the ERS image presents a lower number of pixels with respect to the TerraSAR one: this means that the accuracy in the estimation of the NM will be higher for the TerraSAR image with respect to the ERS one. The considered subset of the amplitude images are shown in Fig. 3, while the estimated NM are shown in Fig. 4 (vertical NM axis is in logarithmic scale) along with the theoretical fully developed speckle NM curve.

Looking to the plots in Fig. 4, it can be noted that the low resolution image NM curve is very close to the theoretical one, demonstrating the effectiveness of the fully developed speckle in modeling this situation. Conversely, the high resolution presents a huge gap from the low resolution scenario and, consequently, from the fully developed speckle hypothesis.

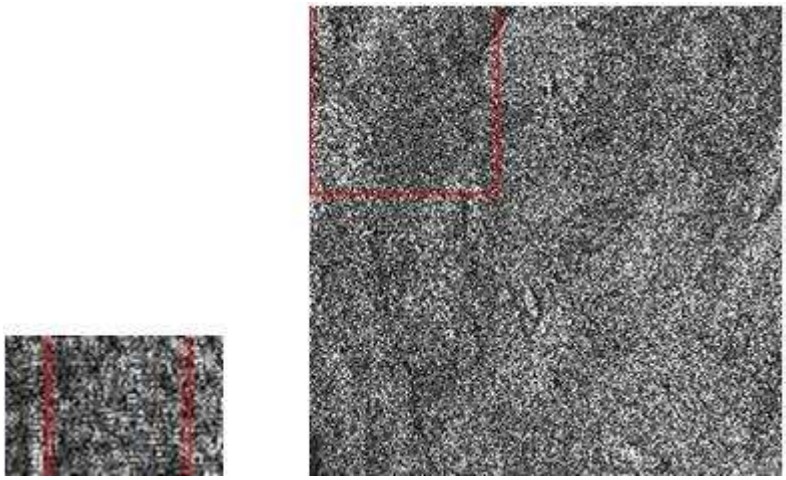

Figure 3 Considered image subsets for the evaluation of normalized moments: ERS image on the left and TerraSAR-X on the right.

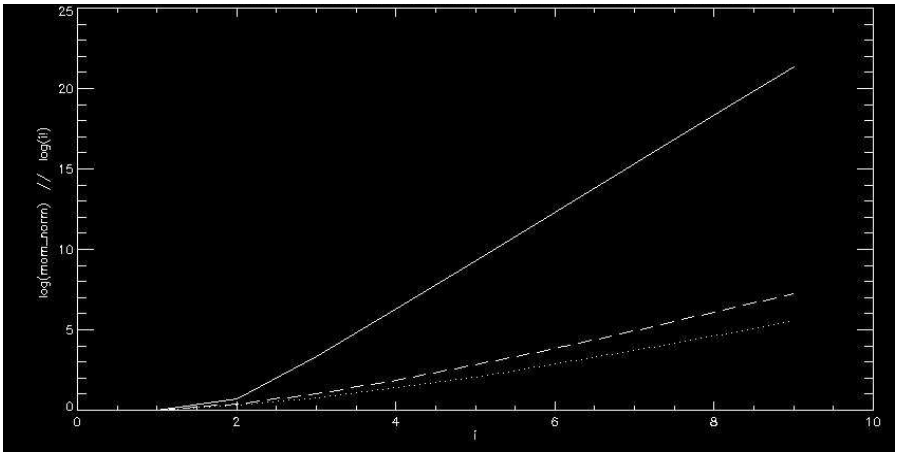

Figure 4 Normalized moments computed on the image subsets shown in Fig.4: the full line is relevant to the TerraSAR image, the dashed one to the ERS image and the dotted line is theoretical NM curve for fully developed speckle.

Hence, the need for new models rises and in Fig. 5 the NM evaluated on a TerraSAR-X image homogeneous subset are shown and compared with the theoretical behavior of the NM in case of fully developed and K-distributed speckle.

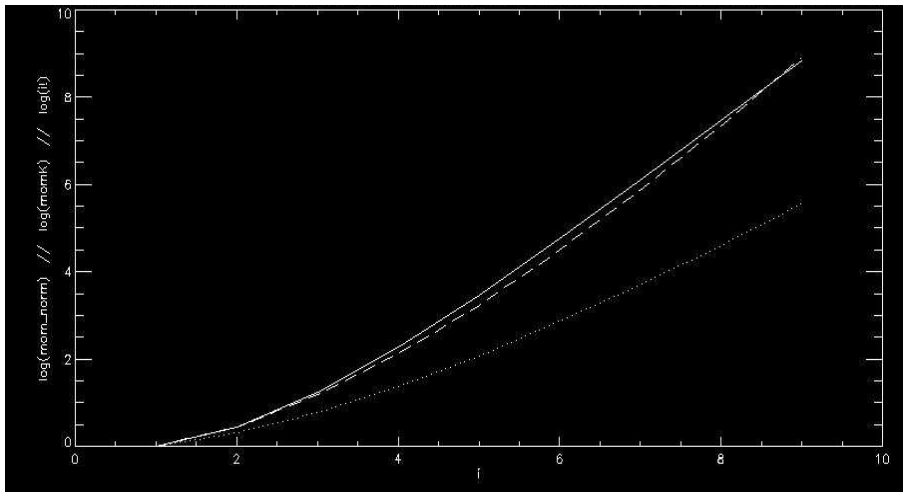

Figure 5 Normalized moments computed on TerraSAR data (full line), compared with the moments of a K-distributed speckle (dashed line) and of a fully developed speckle (dotted line).

It is evident the gap between the NM of the actual image and the theoretical behavior of fully developed speckle; conversely, the fit between the actual data and the K-distributed model is very good.

Note that the two models of speckle presented here are, as far as we know, the only physically-based ones: in fact they are obtained analyzing different situations of *random walks* on the complex plane in which the backscattered field can be represented [4], [6]-[8]. This mean that further developments on this topic could lead to techniques exploiting the noise to recover some properties of the surface, rather than only trying to discard this noise.

The examples presented in this section demonstrate how different sensor resolutions can give rise to completely different phenomena. This is another reason for the development of accurate models in support of information extraction: in these models sensor resolution should appear as a key parameter.

References

[1] G.Franceschetti and R.Lanari; Synthetic Aperture Radar Processing, CRC PRESS, New York, 1999.

[2] R. Touzi, “A review of speckle filtering in the context of estimation theory”, *IEEE Trans. Geosc. Remote Sensing*, vol. 40, no. 11, pp. 2392-2404, Nov. 2002.

[3] G.Franceschetti, M.Migliaccio, D.Riccio, G.Schirinzi, "SARAS: a SAR Raw Signal Simulator", *IEEE Trans. Geosc. Remote Sensing*, vol. 30, no. 1, pp. 110-123, Jan. 1992.

[4] J. W. Goodman, “Some fundamental properties of speckle”, *J. Opt. Soc. Am.*, vol. 66, no. 11, pp. 1145-1150, Nov. 1976.

[5] G. Franceschetti, M. Migliaccio, D. Riccio, "An electromagnetic fractal-based model for the study of the fading", *Radio Sci.*, vol. 31, no. 6, pp. 1749-1759, Nov./Dec.1996.

[6] E. Jakeman, P. N. Pusey, “A model for non-Rayleigh sea echo”, *IEEE Trans. Antennas Propagat.*, vol. 24, no. 6, pp. 806-814, Nov. 1976.

[7] E. Jakeman, P. N. Pusey, “Significance of K distributions in scattering experiments”, *Phys. Rev. Lett.*, vol. 40, no. 9, pp. 546-550, Feb. 1978.

[8] C. J. Olivier, “A model for non-Rayleigh scattering statistics”, *Opt. Acta*, vol. 31, no. 6, pp. 701-722, 1984.

Chapter 2

Direct Models for Natural Surfaces

In Chapter 1 the fundamentals of SAR remote sensing were presented. An extensive discussion on the need for sound physically-based models has been done, pointing out what kind of models is required. A discussion on the role of resolution in the definition of the appropriate models has been reported also through the analysis of actual high resolution data.

In this chapter we examine in detail the models used in this thesis work: in particular, the case of natural terrain and of the sea surface are presented. For each of them both the geometric and the electromagnetic models are described.

2.1 Fractal models

In this section appropriate models for the description of natural terrain surfaces are presented. Fractal models are widely considered the most appropriate to quantitatively describe natural surfaces. In fact, fractal geometry is able to simply account for the non-stationarity of natural surfaces, as well as for their self-affinity [1]-[3].

A fundamental concept of fractal geometry is the*Hausdorff–Besicovitch* (HB) *dimension*, or *fractal dimension*. The definition of HB dimension is based on the concept of the *Hausdorff measure*. A set is said to be fractal if its fractal dimension is greater than its topological one. For instance, a surface is fractal if its fractal dimension D is greater than 2. The fractal dimension is related to the surface roughness: an almost smooth surface has a low (i.e., slightly greater than 2) fractal dimension, whereas an extremely rough surface has a fractal dimension that approaches 3, since it tends to *fill* a volume.

All fractal sets exhibit some form of scale invariance. We recall that a set is *self-similar* if it is invariant (possibly in statistical sense) with respect to a transformation in which all the coordinates are scaled down by the same factor; it is *self-affine* if it is invariant (possibly in statistical sense) with respect to a transformation in which coordinates are scaled down by factors not all equal. As already stated, self-affinity of fractal sets is the key property that makes them particularly useful in describing natural surfaces.

These fundamental properties of natural surfaces are hardly reproduced by classical surface models based on Euclidean geometry. In particular, the second order statistical characterization of the surface can be very inaccurate, if use is made of classical concepts as the *correlation length*: in fact, the lack of a characteristic scale is a key feature of natural profiles, well-known, for example, to earth science researchers.

For scattering evaluation purposes a second order characterization of the surface is necessary [4]. In the fractal case this kind of description is very simple and straightforward, while in the classical case a heuristic choice of the shape of the correlation function has to be performed. The success of fractal geometry in describing natural scenes is also due to the existence of scattering models based on such a description for the surface. It has been demonstrated that the use of fractal scattering models strongly improves the performance in the evaluation of the scattered field.

The combined use of fractal geometrical and electromagnetic models can be used to evaluate the signal received onboard by the SAR system. In the following the fundamentals of these models are provided.

2.1.1 Fractal description of natural surfaces

Many different types of fractal functions have been used in the literature to describe and synthesize natural surfaces [1]-[5]. However, in the contest of this thesis, the geometrical description of the surface has to be adequate to address the problem of electromagnetic scattering. Thus, the ways to describe natural surfaces come to be essentially two.

The first method is to describe the surface as a realization of a *fractional Brownian motion* (fBm) stochastic process. In this case, it is possible to obtain a very simple expression for the mean square value of the field, depending on the fractal parameters of the surface. Conversely it is not possible to compute the (complex) field [4].
Another way to describe fractal surfaces is using the Weierstrass-Mandelbrot (WM) function. The main advantage of using the WM function is that it is possible to obtain an analytical expression of the (complex) scattered field. However, the obtained expression is very involved, and it is not possible to analytically evaluate the (expected) scattered power density [4].

In this work we are interested in the mean square value of the backscattered, which, apart from multiplicative factors, is equal to the Radar Cross Section (RCS). Hence, we use an fBm description of the surface: however, in practical cases fBm surfaces are better synthesized through appropriate techniques based on the use of the WM function. Thus, in the following both WM and fBm surface models are considered; conversely, the scattering problem is addressed only starting from an fBm description for the height profile.

2.1.1.1 Fractional Brownian motion process

The fBm is defined in terms of the probability density function of its height increments: a stochastic process $z(x,y)$ is an fBm surface if, for every x, y, x', y', it satisfies the following relation:

$$\Pr\left\{z(x,y)-z(x',y')<\bar{\zeta}\right\}=\frac{1}{\sqrt{2\pi}s\tau^{H}}\int_{-\infty}^{\bar{\zeta}}\exp\left(-\frac{\zeta^{2}}{2s^{2}\tau^{2H}}\right)d\zeta \qquad (2.1)$$

where τ is the distance between the points (x,y) and (x',y'), and the two parameters that control the fBm behavior are:

- H : the *Hurst coefficient* ($0<H<1$), related to the fractal dimension D by means of the relation $D=3-H$;
- s : the standard deviation, measured in $[m^{(1-H)}]$, of surface increments at unitary distance, a real parameter related to an

fBm characteristic length, the topothesy T, by means of the relation $s = T^{(1-H)}$.

For a given surface the structure function (whose plot is named the variogram), $V(\tau)$, is defined as the mean square increment of elevation points placed at distance τ :

$$V(\tau) = \left\langle \left(z(x,y) - z(x',y') \right)^2 \right\rangle \tag{2.2}$$

The structure function of an fBm surface can be evaluated in terms of the parameters H and s as:

$$V(\tau) = s^2 \tau^{2H} . \tag{2.3}$$

Eq. (2.3) can be written in logarithmic form as:

$$\log V(\tau) = 2 \log s + 2H \log \tau , \tag{2.4}$$

which defines in a log – log plane a linear behavior with slope $2H$, and ordinate intercept $2\log s$.
Due to the non-stationarity of the process, the evaluation of the spectrum is not s trivial issue [6]. Using mathematical instruments as Generalized Fourier Transforms and spatial – scale analysis (for example using wavelet theory), it has been demonstrated [4], [6] that the spectrum $S(k)$ of an isotropic fBm process exhibits a power law behaviour:

$$S(k) = S_o k^{-\alpha} \tag{2.5}$$

wherein the spectral and spatial domain parameters are related by the following relationships:

$$\alpha = 2 + 2H = 8 - 2D , \tag{2.6}$$

$$S_0 = s^2 2^{2H} 2\pi H \frac{\Gamma(1+H)}{\Gamma(1-H)} \tag{2.7}$$

$\Gamma(\cdot)$ being the Gamma function. From the inequalities $0<H<1$ we get $2<\alpha<4$, which defines the range of allowed values for the spectral slope α. Note that also the spectral equation (2.5) provides a linear relation in a $\log(S) - \log(k)$ plane, with parameters related to those of the log-log representation introduced for the variogram.

It is important to note that a surface satisfying Eq. (2.1) for every τ is self-affine on all scales, so that it has details on any arbitrarily small scale and is not differentiable at any point (although it is continuous). Therefore, it cannot be used in electromagnetic scattering problems because the continuity conditions of tangential fields cannot be enforced. Furthermore, such surface is not stationary and suffers from the infinite variance problem (the integral of the power spectrum diverges in the low-frequency range, infrared catastrophe, if $\alpha > 2$, see Eq. (2.5)). Such a surface is also called a *mathematical* fBm surface. However, natural surfaces exhibit a fractal behavior only on a wide but limited range of scales. In addition, the range of scales of interest for a scattering problem is limited on one side by the finite linear size l of the illuminated surface, and on the other by the fact that surface variations on scales much smaller than wavelength λ do not affect the scattered field. Accordingly, we consider *physical* fBm surfaces, i.e., surfaces that satisfy Eq. (2.1) only for $\tau_{min} < \tau < \tau_{max}$, with τ_{max} on the order of l and τ_{min} on the order of $\lambda/10$. If $\tau_{min} << \tau_{max}$, this implies that such surfaces satisfy Eq. (2.5) only in a wide but limited range of spatial frequencies $k_{min} < k < k_{max}$, with $k_{min} = 1/\tau_{max}$ and $k_{max} = 1/\tau_{min}$. That is why these surfaces are also referred to as *band-limited* fBm. It can be demonstrated that band-limited fBm surfaces are stationary (at least in wide sense) and regular. Starting from the definition of such physical fractals is possible to find closed form expressions relating the fractal parameters to some equivalent classical parameter as variance, slope and curvature [4].

An example of fBm surface profile is shown in Fig. 1 (taken from Ref. [7]): self-affinity is clearly illustrated by the sequence of zooms shown in the plots.

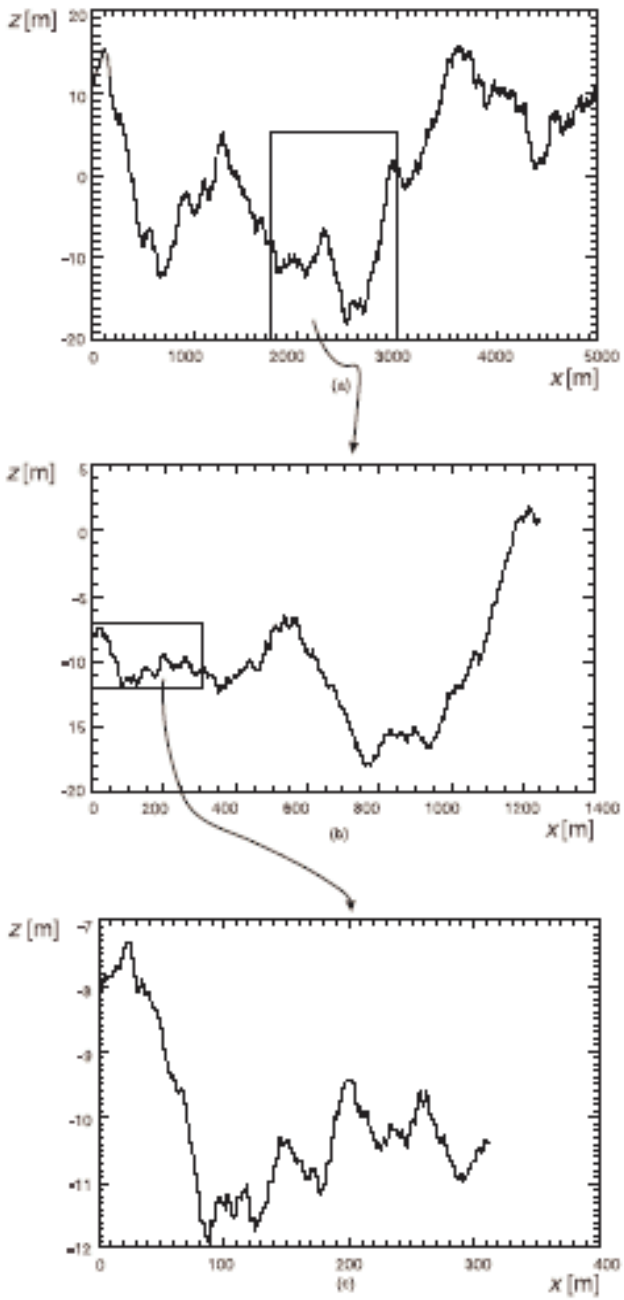

Figure 1 Example of fBm profile: $H = 0.75$; $S_0 = 0.01\ \mathrm{m}^{[2-2H]}$, $l = 5000$ m. (b) and (c) are exploded views of the framed boxes in (a) and (b), respectively.

2.1.1.2 Weierstrass-Mandelbrot function

Among several possible representations of the WM function, one in particular is convenient for modeling the interaction of natural surfaces and electromagnetic waves [2], [8]. We may consider the non-normalized WM function $z(x, y)$ as the superposition of an infinite number of sinusoidal tones, each one characterized by the value of the index p:

$$z(x,y) = B\sum_{p=-\infty}^{\infty} C_p \nu^{-Hp} \sin\left[k_0 \nu^p (x\cos\Psi_p + y\sin\Psi_p) + \Phi_p\right] \quad (2.8)$$

wherein B [m] is the overall amplitude scaling factor, k_0 [m^{-1}] is the wavenumber of the fundamental component (corresponding to $p = 0$), v (greater than 1) is the seed of the geometrical progression that accounts for spectral separation of consecutive components of the surface and $0 < H < 1$ is the Hurst exponent; C_p, Ψ_p and Φ_p are deterministic or random coefficients that account, respectively, for amplitude, direction and phase behavior of each tone.

A discussion on the meaning and on the consequent choice of these coefficients is now in order. If the coefficients C_p are deterministic, they must be all equal and constant, $Cp = C$, so that the tone amplitudes, BCv^{-Hp}, ensure the correct power-law spectral behavior of the fractal function. For random coefficients Cp, the usual choice for their pdf is Gaussian with zero mean and unitary variance. If the coefficients Ψ_p are deterministic, all equal and constant, $\Psi_p = \Psi$, the surface exhibits the fractal behavior only in the direction selected by Ψ (and is constant along the direction orthogonal to it). If the coefficients Ψ_p are uniformly distributed in $[-\pi, \pi]$, the WM function is isotropic in statistical sense; any other choice leads to an anisotropic surface. If the coefficients Φ_p are deterministic, they are usually selected to ensure that the WM function exhibits the self-affine behavior.

If the coefficients Φ_p are random, they are usually chosen uniformly distributed in $[-\pi, \pi]$, and the *zero-set* of the WM function (i.e., the set of points of intersection with the plane $z = 0$) is nondeterministic.

In case of a random WM function, the random coefficients, C_p, Ψ_p and Φ_p, are usually assumed to be mutually independent.

Equation (2.8) exhibits a non-integer fractal dimension D as soon as v is irrational and the Hurst exponent is related to the fractal dimension D as

$$D = 3 - H \,. \tag{2.9}$$

In case of random coefficients, the WM function holds the self-affine behavior only for a scaling factor $r = v^n$. Whenever v tends to 1 the WM function approaches the self-affine behavior in the statistical sense.

A physical WM function can be obtained by just limiting the summation extent to P tones, thus obtaining band-limited WM surfaces:

$$z(x,y) = B\sum_{p=0}^{P-1} C_p v^{-Hp} \sin\left[k_0 v^p (x\cos\Psi_p + y\sin\Psi_p) + \Phi_p \right] \tag{2.10}$$

As in the case of fBm, use of band-limited WM surfaces is physically justified by the fact that any scattering measurement is limited to a finite set of scales. Let (X, Y) be the antenna footprint over the surface. The lowest spatial frequency of the surface, $k_0/2\pi$, is linked to the footprint diameter $\sqrt{X^2+Y^2}$, while the upper one $k_0 v^{p-1}/2\pi$ is related to the electromagnetic wavelength λ, possibly through an appropriate safety factor χ in the range [0,1], usually set equal to 0.1. Accordingly, we can set

$$k_{\min} = k_0 = \frac{2\pi}{\sqrt{X^2+Y^2}}\,, \tag{2.11}$$

$$k_{\max} = k_0 v^{p-1} = \frac{2\pi}{\chi\lambda}\,. \tag{2.12}$$

Relations (2.11) and (2.12) can be used to determine the number of tones P needed to effectively describe the physical WM of interest:

$$P = \left\lceil \frac{\ln\left(\sqrt{X^2 + Y^2} / \chi\lambda\right)}{\ln \nu} \right\rceil + 1 \tag{2.13}$$

where the $\lceil \cdot \rceil$ operator is the ceiling defined so as to take the upper integer of its argument.

Also in this case it is possible to obtain a relation between the parameters of the WM function and classical surface parameters [4].

2.1.1.3 Connection between WM and fBm surfaces

As a matter of fact, it is not trivial to obtain realizations of fBm sample functions characterized by H and S_0 parameters; conversely, the WM function is easily computed via simple summation of sinusoidal tones. For this reason it is useful to establish a relation between the fBm and the WM parameters in such a way that an fBm surface can be synthesized via an opportune WM function. As for the Hurst parameter, it is simple to verify that it is equal to the H value in (2.8): hence, we need only a relation for the amplitude factors S_0 and B.

Looking at Eq. (2.8), it can be noted that, under some hypotheses, the WM could be intended as a sampled representation of an fBm. Hence, the required connection can be established by comparing the corresponding power spectra and checking to what extent the former is a sampled representation of the latter at the discrete spatial frequencies $k_p = k_0 \nu^p$.

Dividing the spectral plane k_x, k_y into concentric annular regions of radii ($k_p \nu^{1/2}$, $k_p \nu^{-1/2}$) respectively, and computing the spectral power within each annular region pertinent to WM and fBm surface description, is possible to obtain the following relations involving the parameters of interest [4]:

$$B^2 = \frac{S_0}{2\pi H} k_0^{-2H} \left(\nu^H - \nu^{-H}\right) \tag{2.14}$$

which for ν approaching 1 (i.e., when the spectrum of the WM becomes almost continuous) can be written as:

$$B^2 = \frac{1}{\pi} S_0 k_0^{2H} (\nu - 1). \tag{2.15}$$

Summarizing, we can say that the WM function and the fBm process both posses the same Hurst parameter and hence, at least in the limit $\nu \to 1$, the same fractal dimension. This is consistent with the fact that the equivalent power spectral decay of the WM function and the power spectral decay of the corresponding fBm process are the same. Finally, if B is selected according to Eq. (2.14), then the power content of the WM function and the equivalent fBm process are equal on appropriate spectral intervals; in the limit of $\nu \to 1$ this last result is valid on any spectral interval.

In Fig. 2 (taken from Ref. [7]) we plot WM profiles for fixed values of H, k_0, and for different values of ν and B. It is visually evident from comparison of Figs. 1 and 2 that if ν is small enough (a value equal to the Neper number e may be sufficient), then Eq. (2.8) can be used to generate an fBm sample profile.

2.1.2 Scattering from fractional Brownian surfaces

An extensive discussion on scattering models is beyond the scope of this thesis work. In this section we will only provide the final results of the evaluation of closed form analytical solutions for the scattering problem in case the observed surface is described as an fBm process.

Two models are of interest in the following, the Physical Optics (PO) solution and the Small Perturbation Method (SPM). In the following their rationale is exposed.

2.1.2.1 Physical Optics solution

In order to evaluate the scattered power density we need to evaluate the mean square value of the scattered field, which after some manipulation and a coordinate transformation, can be written as an integral involving the structure function of the considered surface [4].

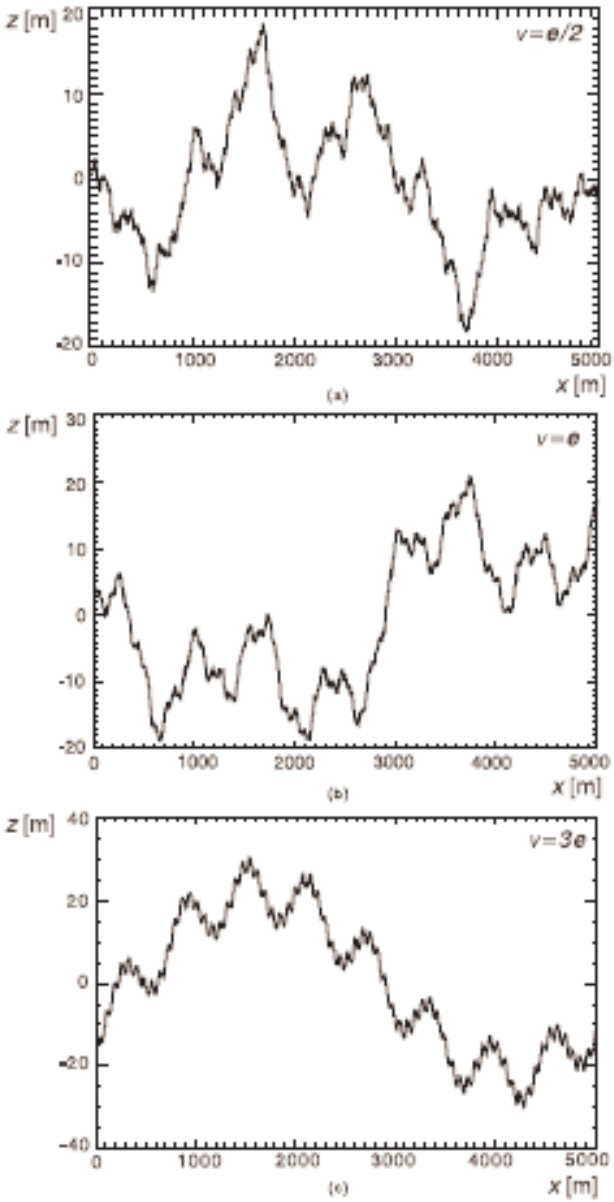

Figure 2 Examples of WM profiles: $H = 0.75$, $l = 5000$ m; (a) $v = e/2$ and $B = 4.70$ m; (b) $v = e$ and $B = 8.85$ m; (c) $v = 3e$ and $B = 14.8$ m. In all three cases Eq. (2.8), modified to account for one-dimensional profiles, leads to an equivalent fBm process with $H = 0.75$ and $S_0 = 0.01\ \mathrm{m}^{[2-2H]}$.

The use of the expression in Eq. (2.3) allows the evaluation of two different closed form solutions for the scattering problem. The corresponding expressions for the Radar Cross Section (RCS) are the following [9], [2]:

$$\sigma_{pp}^{0} = \frac{\left|R_p(\vartheta)\right|^2 k^2 T^2 \cos^2(\vartheta)}{H} \sum_{n=0}^{\infty} \frac{(-1)^n \Gamma\left(\frac{n+1}{H}\right)}{(n!)^2} \cdot \frac{(kT \sin\vartheta)^n}{\left(\sqrt{2}kT\cos\vartheta\right)^{\frac{2n+2}{H}}} \tag{2.16}$$

for $H \geq 1/2$ and

$$\sigma_{pp}^{0} = \left|R_p(\vartheta)\right|^2 k^2 T^2 \cos^2(\vartheta) H \sum_{n=0}^{\infty} \frac{(-1)^{n+1} n\Gamma(1+nH)}{n!\Gamma(1-nH)} \cdot \frac{\left(\sqrt{2}kT\cos\vartheta\right)^{2n}}{\left(\sqrt{2}kT\sin\vartheta\right)^{2nH+2}} \tag{2.17}$$

for $0 < H \leq 1/2$. In Eq. (2.16) and (2.17) ϑ is the local incidence angle of the mean plane and $R_p(\vartheta)$ is the Fresnel reflection coefficient and the RCS is computed as

$$\sigma_{pq}^{0} = \frac{4\pi R_0^2 < \left|E_q^{(s)}\right|^2 >}{A\left|E_p^{(i)}\right|^2} \tag{2.18}$$

where $E_p^{(i)}$ and $E_q^{(s)}$ are the incident and the scattered field computed in the same direction (p and q standing for the considered polarizations), R_0 is the distance with the receiver and A is the area of the illuminated surface.

A discussion on the validity limits of this model is now in order. To obtain the expressions in Eq. (2.16) and (2.17) two hypotheses have been done: the validity of the Kirchhoff Approach (KA) and a small slope approximation. As for the KA, it holds if the mean radius of curvature of the surface is much greater than the wavelength of the incident field. Conversely, the small slope approximation holds if the

rms slope is much smaller than unity. As we mentioned in the previous sections, it is possible to evaluate curvature and rms slope of fBm surfaces introducing the concept of band-limited fractals: in this way, it is possible to assess the validity limits of the PO model in terms of the fractal parameters of the surface. Obviously, the expression of these validity limits will be strongly dependent on the particular type of physical fractal used in the description of the surface.

Finally, let us note that the series in Eq. (2.16) and (2.17) can be truncated to a finite number of terms, for computer evaluation purposes. In fact, in practical cases the convergence rate of the two series (or at least of one of the two series at a time) is high and only few terms will be needed for the computation of the RCS [4].

2.1.2.2 Small Perturbation Method

As we have seen, using the KA is possible to obtain a closed form expression for the mean square value of the backscattered field. Unfortunately, the computation of a series is required to obtain the desired RCS. A much simpler result can be obtained by employing the SPM. This method is based on the Rayleigh hypothesis and on a surface field series expansion, and can be used if surface height variations are small compared to the wavelength [9], [4].

The RCS in this case can be written as follows:

$$\sigma_{pq}^{0} = 8k^{4}\cos^{4}\vartheta\ \left|\beta_{pq}\right|^{2}\ 2\pi S_{0}\Big/\left(2k\sin\vartheta\right)^{\alpha} \tag{2.19}$$

where β_{pq} is a function accounting for the field polarization, ϑ is the local incident angle and k the electromagnetic wavenumber.

Note that Eq. (2.19) diverges at normal incidence. Such a condition does not allow the implementation of the model in practical cases. Therefore, in order to overcome this problem, it is possible to use a transition function for low incidence angles, based on the previously presented Physical Optics solution to the Kirchhoff Approach.

Like in the PO case, validity limits can be evaluated introducing equivalent classical parameters for the fBm physical surface [4].

2.2 The ocean surface

In this section we focus on a different kind of natural surface: sea surface. Oceans are nonlinear dynamic systems, whose physics is governed by very complex laws. Description of ocean surface waves is the most relevant branch of oceanography for electromagnetic sea sensing.

Surface waves are found in the ocean with wavelengths ranging from the hundred of meters to the millimeter scale. The ocean wave range is usually divided into long (several hundred meters length), intermediate (tens of meters length), and short (less than one meter) waves. In the literature, the ocean waves are also classified according to the physical phenomenon that dominates their formation: long and intermediate waves are usually referred to as gravity waves; conversely, the range of short waves includes the shortest gravity waves, and gravity-capillary (one centimeter to decimeters) and capillary (less than 1 cm) waves.

Hereafter, we will focus on a particular sea status: the so called fully developed sea. In fact, models for other sea conditions (for example, inshore sea) are unavailable or, at least, very involved. Conversely, the presented sea surface model allows the evaluation of the RCS as a function of key physical parameters, such as wind speed and potential presence of pollutants on the surface.

The basic backscattering mechanism in this case, at least for intermediate incidence angles and appropriate environmental conditions, is the Bragg one. However, it must be emphasized that when the resolution cell is small with respect to the ocean backscattering wavelength, i.e., it no longer features a collection of scatterers and/or we deal with low grazing angles, the microwave backscattering is not of the Bragg type and different models have to be suggested and investigated.

One of the most important causes of pollution in the ocean is the intensive oil emission onto the water. Natural oil is present in the ocean due to natural phenomena, but many statistic studies showed that human activities change the percentage of oil in water, sometimes with dramatic effects. Oil spills caused by accidental or intentional emissions interact with the local marine ecosystems and, by modifying the delicate air–sea balance, exhibit great influence on large- and

short-scale phenomena. Remote sensing has proved to be a powerful tool to study ocean dynamics and detect oil spills. Optical, radiometric, and radar systems have been employed for the detection of oil slicks in the sea. In particular, SAR systems have been shown to be very useful.

Obviously, the purpose of this work is not to give a general assessment of the above theories, but just to present their rationale, trying to provide a simulation-oriented approach. Thus, in the following the physics of the problem will be discussed without stressing the unnecessary mathematical detail.

2.2.1 Fully developed sea surface spectrum

The first definition of a fully developed sea surface spectrum is probably due to Pierson and Moskovitz. They assumed that if the wind blew steadily for a long time over a large area, the waves would come into equilibrium with the wind. This is the concept of a fully developed sea [10]-[13].

Loosely speaking, when the wind blows over the ocean surface, capillary waves rise first. Then, the capillary waves transfer energy to waves with longer wavelength. This phenomenon continues until equilibrium is reached (fully developed sea). Such equilibrium depends on the wind strength. When the wind stops blowing, the short waves decrease quickly, while the long waves propagate far from their source (and, in this case, are usually referred to as swell). Accordingly, long waves are generated by strong far winds, at variance of short waves, which are generated by local winds. It can be concluded that their directions of propagation are usually different and that they interact in a very complex way. Besides, it has been demonstrated that intermediate and long waves modulate the amplitude of the short waves. Let us briefly describe the different parts of the sea spectrum.

The long wave can be seen as a realization of a random process describing a swell profile at a fixed time: central wavenumber, amplitude, and bandwidth of its spectrum are the parameters of interest in this case. They depend on the far wind intensity and direction and on the fetch area. This part of the spectrum is basically described by a wave-packet.

With regard to short waves, we consider the Pierson–Moskovitz spectrum. In particular, is interesting to note that the short gravity range of this spectrum exhibits a power law behavior and is frequently modeled as fractal. This part of the spectrum is also the one used in the computation of the scattering, where Bragg mechanism selects resonant waves in this range of wavenumber. In this case wind speed is a fundamental parameter involved in the definition of the spectrum [14].

As we noted above, the different spectral components interact one with each other: thus, to complete the description of the surface and account for its time-varying nature we need a dispersion relation for the long wave spectrum [14].

However, an exhaustive discussion on problems involved in the whole ocean spectrum definition, use, and meaning is beyond the aim of this paper and can be found in the specialized literature, for example in Ref. [10]-[13].

2.2.2 Bragg scattering

As already noted, the key mechanism involved in the interaction between the electromagnetic field and the sea surface (at least a fully developed one) is Bragg scattering. It is based on the observation that main contributions to the backscattered field are provided by the ripple spectral components whose wavelength is of the same order of magnitude of the incident electromagnetic wavelength. Since the height of sea waves is much smaller than their wavelength (unless breaking waves are considered), then the height of ripple spectral components involved in the scattering mechanism must be much smaller than the electromagnetic wavelength, too [14].

This allows finding a direct dependence of the RCS from the resonant components of the sea spectrum $W\left(\bar{k}_x, \bar{k}_y\right)$ with:

$$\begin{cases} \bar{k}_x = \dfrac{4\pi}{\lambda}\delta_x \cos\vartheta_i \\ \bar{k}_y = \dfrac{4\pi}{\lambda}\left(\sin\vartheta_i + \delta_y \cos\vartheta_i\right) \end{cases} \tag{2.20}$$

where δ_x and δ_y are the slopes of the sea macroscopic surface in the two directions and ϑ_i is the local incidence angle.

Equations (2.20) clearly show that, according to the Bragg phenomenon, the SAR sensor acts as a frequency selector; hence, the ocean waves that contribute to the scattering are only those resonant with the wavenumbers such that Eq. (2.20) holds.

2.2.3 Effects of oil pollutants on sea surface

Hereafter, we briefly discuss the ocean spectrum dependence on the presence of oil [15]-[19].

The presence of oil on the water surface reduces surface tension and friction between wind and liquid surface: the higher the oil percentage, the stronger the reduction effect. This means that the wind can transfer a smaller energy to capillary waves in oil-slick-covered areas than in free-water areas. In addition, viscous dissipation increases. All this causes a decrement of the capillary spectrum intensity, which, as presented above, plays a dominant role in the scattering mechanism. Then, according to what we said in the previous sub-section, a weaker electromagnetic return from areas affected by oil presence is expected, which causes darker areas in SAR images.

To quantify the abovementioned phenomenon a model based on the Marangoni theory and on a nonlinear energy transfer theory can be used. This model arises from a theoretical physical–chemical approach and provides a reasonable physical interpretation to a typical behavior of the wave damping in a range of wavenumber of great interest for SAR applications. According to Marangoni, surfaces covered by a slick can carry two kinds of waves: the gravity-capillary and the Marangoni waves. Marangoni waves are related to surface tension gradients, caused by the oil film visco-elastic reaction to the sea surface deformations. At variance of gravity-capillary waves, Marangoni waves are longitudinal. When Marangoni and gravity-capillary waves share the same wavenumber for a given frequency, a maximum in the damping occurs.

Thus, it is possible to obtain an analytical expression for the damping coefficient which depends on the visco-elastic of the considered oil.

However, the dampening caused by Marangoni waves is not sufficient to completely explain sea surface spectrum variations in the presence of oil. As a matter of fact, according to Marangoni theory, oil slicks influence ocean waves with wavelength only lower than 1 m, whereas experience suggests that the whole spectrum is affected by the oil presence.

In fact, when an external input acts on the ocean and changes its shape, the system reacts by spreading uniformly the energy through its whole spectrum via wave–wave nonlinear interactions. Hence, when an oil slick causes a strong spectrum damping around the Marangoni resonant wavelength, longer and shorter waves transfer part of their energy to the waves in the resonant spectral region, via the nonlinear wave interaction phenomenon. This is the reason why, although the damping effect directly acts only on the short waves, longer waves also are influenced by the presence of oil. Such a wave–wave interaction mechanism is strongly influenced by the wind; hence, the higher the wind intensity, the higher the energy spreading effect.

All the phenomena described above can be used to obtain a closed form expression for the RCS also in presence of oil. Most important, we found a way to directly relate, though via strongly non-linear relations, the backscattered signal to physical, chemical and environmental properties, which are all potentially retrievable through inversion of these direct models. Another key result is that we can account for the presence of any kind of oil on the sea surface only by knowing its physical-chemical properties.

All the models described in this last section have been effectively used to develop the SAR ocean simulator presented in Ref. [15], which is able to simulate also the presence of oil over some portion of the image.

References

[1] B.B. Mandelbrot, *The Fractal Geometry of Nature*, W.H.Freeman & C., New York, USA, 1983.

[2] K. Falconer, *Fractal Geometry*, Chichester, John Wiley & Sons, England, 1989.

[3] J.S. Feder, *Fractals*, Plenum Press, New York, USA, 1988.

[4] G. Franceschetti, D. Riccio, *Scattering, Natural Surfaces and Fractals*. Academic Press, Burlington (MA), USA, 2007.

[5] R. F. Voss, “Random Fractal Forgeries”, in *Fundamental Algorithms for Computer Graphics*, edited by R. A. Earnshaw, pp. 805-835, Springer-Verlag, New York NY, USA,1985.

[6] P. Flandrin, “On the spectrum of fractional Brownian motions”, *IEEE Trans. Inform. Theory.*, vol.35, pp. 197–199, 1989.

[7] G. Franceschetti, A. Iodice, D. Riccio, "Fractal Models for Scattering from Natural Surfaces", Invited Chapter in *Scattering*, R. Pike, P. Sabatier, eds., Academic Press, London (UK), pp. 467-485, Sept. 2001.

[8] M.V. Berry and Z.V. Lewis ,"On the Weierstrass-Mandelbrot Fractal Function", *Proc. R. Soc. Lond.*, A, 370, pp.459-484, 1980.

[9] A. K. Fung, *Microwave Scattering and Emission. Models and Their Applications*. Artech House, Norwood, MA, 1994.

[10] J. R. Apel, *Principles of Ocean Physics*. San Diego, CA: Academic, 1988.

[11] B. Kinsman, *Wind Waves*. Mineola, NY: Dover, 1983.

[12] G. Neumann and W.J. Pierson, *Principles of Physical Oceanography*. Englewood Cliffs, NJ: Prentice-Hall, 1996.

[13] A. Defant, *Physical Oceanography*. New York: Pergamon, 1961, vol. I-II.

[14] G. Franceschetti, M. Migliaccio, and D. Riccio, “On ocean SAR raw signal simulation,” *IEEE Trans. Geosci. Remote Sensing*, vol. 36, pp. 84–100, Jan. 1998.

[15] G. Franceschetti, A. Iodice, D. Riccio, G. Ruello, R. Siviero, “SAR Raw Signal Simulation of Oil Slicks in Ocean Environment”, *IEEE Trans. Geosci. Remote Sens.*,vol.40, n.9, pp. 1935-1949, Sep. 2002.

[16] W. Alpers and H. Huhnerfuss, “The damping of ocean waves by surface films: A new look at an old problem,” *J. Geophys. Res.*, vol. 94, pp. 6251–6265, 1989.

[17] V. G. Levich, *Physico-Chemical Hydrodynamics*. Englewood Cliffs, NJ: Prentice-Hall, 1962.

[18] P. P. Lombardini, F. Piazzese, and R. Cini, "The Marangoni wave ripples on an air-water interface covered by a spreading film," *Nuovo Cimento*, vol. 5C, no. 2, 1982.

[19] B. Fiscella, P. P. Lombardini, P. Trivero, and R. Cini, "Ripple damping on water surface covered by a spreading film: Theory and experiment," *Nuovo Cimento*, vol. 8C, no. 5, 1985.

Chapter 3

SAR Simulation Tools

Several approaches devoted to define instruments and tools for data interpretation were presented in literature. Most of them are based on empirical analyses of remote sensing data, essentially driven by user needs. For an efficient information extraction, as we argued in Chapter 1, we need physical models: some of them were reviewed in the previous chapter.

In this chapter we present novel results concerning the development of model-based automatic techniques for the analysis of SAR amplitude images.

In the first section, a fractal framework for the simulation of SAR images relevant to simulated disaster scenarios is introduced. Such an instrument can be used to increase the comprehension of the physical mechanisms underlying radar image formation in case of disasters. In, fact, the main problem of the scientist working on the development of remote sensing techniques for disaster monitoring is the lack or the limitedness of an accurate ground truth. The proposed simulator allows performing parametric studies on canonical disasters scenarios with a perfectly known ground truth. Furthermore, it can be used to obtain images relevant to both pre- and post-crisis situations, providing the possibility to develop a test bed of simulated images to be used for the testing of change detection techniques. Relevant case studies are presented with regard to different kinds of natural disasters. Finally, a novel change detection technique based on the estimation of significant parameters and supported by fractal concepts is described.

In the second section, new tools for the simulation and analysis of ocean scenes covered with oil slicks are presented. The produced images have been used for the testing of novel fractal and radiometric techniques for the identification of oil slicks and their discrimination from look-alike (for example, wind faults).

3.1 A fractal simulation and analysis chain

Human beings live in an environment in continuous evolution with a large number of physical phenomena which are potentially dangerous for their life. Remote sensing sensors provide a great amount of data to be used in disaster prevention, risk evaluation, damage estimation and aid organization. However, practical use of these data is often limited by the lack of efficient, possibly unsupervised, tools for the retrieving of effective information to be employed in the crisis and post-crisis phases.

Several approaches devoted to define instruments and tools for data interpretation were presented in literature, showing, at least in principle, the potentiality of satellite and aerial technique for the monitoring and eventually prevention, of natural (flooding [1]-[2], volcanic risk [3], landslides [4], etc.) and human-made disasters (oil spills, fires, etc.). Most of these approaches are based on empirical analyses of remotely sensing data, essentially driven by user needs. These analyses are generally supervised; and, to be effective, it is often required that the supervisor holds a remarkable level of competence with reference both to the remote sensing sensors (and data), and to the effects of different disasters on the environment.

Among remote sensing sensors, the imaging ones take the advantage of generating synoptic views of the area under observation; in this case, the rationale for the feature identification techniques is generally based on the concepts of image texture analysis. Textures on remotely sensed images are related to morphological and geological features, land use and social organization of the observed scene. An expert user can identify significant classes of human signatures, as ordered patterns which are well described within the Euclidean geometry, and distinguish them from natural features, that conversely hold self-similar characteristics thus being governed by non-Euclidean laws. When a disaster occurs, the scenario of the observed scene dramatically changes, and remote sensing instruments should be, at least in principle, able to detect the changes in the scenes. As a matter of fact, man-made structures can be damaged thus (partially) losing their Euclidean properties; alternatively, some natural features can be modified thus changing the characteristics of their non-Euclidean

statistics. An example for the first happening is provided by images of urban areas stricken by earthquakes, where some chaotic textures appear and Euclidean pattern are mixed with self-similar ones. Examples for the second happening are provided by images of a flooding in rural areas or a volcano eruption; these natural disasters modify (according to different rules) the surface profile from scales smaller than the sensor coverage but comparable to the sensor resolution, up to scales comparable to the electromagnetic wavelength.

Then, a fundamental aid in managing post-crisis analysis can be given by unsupervised, or semi-unsupervised tools for interpretation of geometrical features in remotely sensed images: to develop these tools it is crucial to introduce appropriate models to understand and quantitatively describe the physical phenomena that govern the modification of the scenario textures, thus providing a fundamental background to plan any powerful instruments to retrieve the information of interest.

As we have seen in the previous chapter, the fractal geometry has the required characteristics to manage the problem at hand. Therefore, fractal based instruments are appropriate candidates for the retrieval of the significant physical parameters from remotely sensed images. In this section, we present a novel fractal framework, based on direct and inverse models, to facilitate the disaster monitoring from SAR images. In particular, we propose the combined use of an appropriate SAR raw signal simulator with fractal based models and tools.

As for the direct chain, fractal geometrical models are employed to correctly represent the imaged surfaces and fractal scattering models are employed to evaluate the reflectivity function of the natural scene under observation [7]-[8], in agreement to what we saw in the previous chapter. The evaluation of the scattering requires the knowledge of the fractal parameters of the area. Some techniques have been reported in the open literature for the retrieval of the fractal parameters from a given two-dimensional data set, most of them relying on the fractional Brownian model.

The reflectivity function is employed to simulate the SAR raw signal and the relative SAR image, as described in Chapter 1.

As for the inverse chain, in the open literature most of the change detection algorithms are based on ratioing and differencing on

the magnitude of the signal return between pre- and post-crisis scenario [9]-[10]. Fractal tools could be employed for retrieving SAR properties of the SAR images and to develop change detection algorithms based on differencing and ratioing between parameters with a physical meaning. Anyway, these techniques have been mainly proposed with reference to fractal surfaces, thus they quite conveniently apply to Digital Elevation Model (DEM); conversely, their use in case of images of the fractal surface is sometimes questionable. However, these methods present a major problem for remote sensing applications: the estimation is effective only in presence of data equally sampled in both directions. In the following a solution for the problem is proposed.

Such an approach calls for appropriate discussion on the *fractality* of SAR images and on the possibility to retrieve the fractal parameters of the surface by analysing its radar image. In the next chapter a novel analytical closed-form solution will be presented, clarifying the nature of this inverse problem.

In the following a comparison between the SAR raw signal simulator and actual images allows the validation of the whole direct chain. In addition, the direct chain is used to create canonical disasters in order to develop ad hoc solutions for two simulated case studies: a flooding and a volcano eruption.

3.1.1 Fractal framework assessment

The framework makes use of some tools which are here described in terms of input and output data, as well as of employed models and algorithms.

Monitoring of each type of possible disaster calls for appropriate remote sensor coverage, temporal and spatial resolution scales, and sensitivity.

Sensor coverage and sensitivity are somehow dual concepts. Sensor coverage allows focusing on the entire area involved in the disaster so that large scale phenomena can be monitored. Sensor sensitivity is here refereed to the employed electromagnetic wavelength and can be related to the scene spatial scales that mainly affect the remotely sensed data, thus providing information on the small scale phenomena. Temporal resolution fixes the time for

obtaining post-crisis data and the average temporal lag between pre- and post-crisis data. Spatial resolution allows monitoring the disaster at a significant scale with respect to the observed feature. This scale is set at an intermediate level between the sensor coverage and the electromagnetic wavelength.

With respect to above mentioned parameters, spaceborne and airborne SAR data provide a unique tool to monitor several types of disasters. SAR coverage allows imaging Earth at a regional scale which is typical of most of possible disasters. SAR sensitivity depends on the backscattering properties at microwaves, thus being related to the geometrical properties of the scene under survey at centimetric and metric scales. Acquired SAR data exhibit a spatial resolution that can be employed to monitor the geometrical properties at scales ranging from 1 meter to 1 kilometer. Finally, the new generation of spaceborne sensors is conceived to reduce the temporal resolution from days to hours, just as required for an efficient monitoring, (and support controlling) of major natural and human-made disasters. Then, SAR images, with respect to optical ones, exhibit an emphasized dependence on the observed geometrical features on spatial scales ranging from several kilometres to some centimetres.

This short and general discussion provides the major motivation to propose a fractal framework for the study of disasters by means of SAR images. Fractal geometry provides the appropriate "environment" to deal with geometric features that extend in such a wide range of scales. The fractal framework we propose is then based on the following tools.

1. A fractal inverse geometrical tool (IGT) to retrieve the fractal parameters from the surface profile of the scene under analysis.

Input of this tool is an (original) DEM of the scene under analysis. This DEM can be acquired by aero-photogrammetric campaigns or interferometric SAR data; it should be relevant to the entire area under analysis and should be sampled with spacing as closer as possible to the SAR resolution. In general a coarse version of these DEMs can be provided by the data from the Shuttle Radar Topography Mission (SRTM). The outputs of this tool are the maps containing the fractal parameters evaluated in

each point of the original DEM of the scene. The tool we propose is based on the fBm model for the DEM.

2. A fractal interpolation tool (FIT) to obtain the surface profile sampled according to the resolutions of the considered SAR sensor and stochastically described at the scales comparable to the employed wavelength [11], [12].
Input for this tool are the original DEM and the maps of the fractal parameters evaluated by the tool described at step 1. Output is a realisation of the macroscopic DEM at the SAR resolution scale and parameters of the microscopic DEM at SAR wavelength scales to be used in the SAR raw data simulator. At the microscopic scale only the fractal parameters are required by the scattering models, and the fBm model is employed to fix these fractal parameters equals to those estimated at the original scale thus performing a stochastic interpolation of the scene profile up to scale typical of the electromagnetic wavelength.

3. A SAR simulator (SARAS) that makes use of fractal direct scattering formula to generate raw signals and images relevant to the scene under analysis.
Main inputs of this tool are the DEM of the scene sampled at the SAR resolution scale and the fractal parameters at the SAR wavelength scale. This tool evaluates for each portion of the scene the backscattering via a direct scattering formula and projects this result onto the azimuth-slant range coordinate system. This tool employs an fBm model for the surface; the tool can alternatively employ Physical Optics (PO) or Small Perturbation Method (SPM) fractal based solutions for scattering, whose fundamentals were reported in the previous chapter.

A disaster brings significant changes in the geometrical properties of the affected scene. As an example, the roughness of a flooded area is usually lower than before the event, while an inhabited area affected by an earthquake will lose the ordered organization typical of built-up quarters. As presented in Chapter 2, fractal geometry accounts for the irregularity of the surfaces, therefore its use is widely suggested for change monitoring.

In this work we extended the variogram method (which estimates the fractal parameters via a linear regression on the log – log plot of the variogram) to deal with not equally spaced data. Note that, if the data are equally spaced, the number of points with the same relative distances is greater with respect to the case of non-equally spaced samples. In order to reduce this effect we used the Otsu linearity index.

This new tool can perform estimation of pseudo-fractal parameters (for the moment, we don't know whether the image of a fractal is fractal or not) on the final image: we don't know precisely (analytically) how these parameters are related to the fractal parameters of the surface, but, anyway, we expect them to be related.

The SARAS simulator, introduced in Chapter 1, is here modified to allow simulation with fractal and electromagnetic parameters varying all over the scene. In fact, in the study of simulated disasters we will need to change these parameters on the zone hit by the disaster.

3.1.2 Case studies

In the following significant case studies are presented, to assess the performances of the proposed framework.

3.1.2.1 Comparison with actual data

The region of interest is the area of Maratea (39°59'N 15°42'E), South of Italy, a coastal area surrounded by steep mountains. A digital elevation model (DEM) of a 20 x 20 Km^2 area, with 20 x 20 m^2 pixel spacing was available for the considered area, as well as an ERS-1 C-band SAR image, acquired in descending orbit on the 30 of January 1996, with a view angle of 24.88°.

As first, we used our DEM as input for the SARAS simulator, in order to compare the simulated with the ERS-1 image. The DEM was interpolated via the FIT procedure on a 3.99 x 19.93 m^2 spaced grid, in accordance with the ERS acquisition geometry. A pictorial view of the interpolated DEM is shown in Fig. 1, with an observation angle of 24.88°, so that it reproduces the scenario seen by an observer on the ERS-1 satellite.

In Fig. 2 the DEM grey scale representation is provided. Note that the highest mountain (corresponding to the brightest area) has a top altitude of 1506.45m. Columns of the image represent equi-azimuth pixels.

In order to use the presented DEM as input for the SARAS, the description of the scales at the order of the incident wavelength (5 cm for ERS-2 sensor), is needed. The fractal parameters of a natural surface are independent of the scale at which we measure them; therefore, we retrieved the microscopic fractal parameters from the DEM, via the IGT. We present the fractal dimension *D* and the *s* parameter estimated by the reference DEM in Fig. 3 and 4, respectively. Note that the *s* map allows an identification of topographical characteristics, like rivers, or mountains.

Once the long and short scale characterization is provided, it is possible to perform the SARAS simulation of the image generated by the ERS-1 sensor.

The image obtained from the simulated raw signal via standard processing, is presented in Figure 5a and compared with the actual image provided by the ERS-1 SAR. The images are averaged with a 2 x 10 multi-look, so that the presented image resolution in azimuth – slant range is 39.86 x 15.81 m^2, which corresponds to an azimuth – ground range square pixel (39.86 x 37.58 m^2). A visual comparison shows the capacity of the simulator of reproducing the main characteristics of the SAR image, suggesting the use of the SARAS as support for SAR actual image interpretation.

The presented results suggest the use of the SARAS for simulating canonical scenarios to be used as test-bed for the validation of change detection techniques. Therefore, we simulated two crisis-scenarios, one relative to a flooding of the area adjacent to the highest mountain of the region of interest, another relative to a volcano eruption. In both the cases, the previous simulation is considered as the pre-crisis scenario, and it is use as reference for fractal change detection approaches, as detailed in the following.

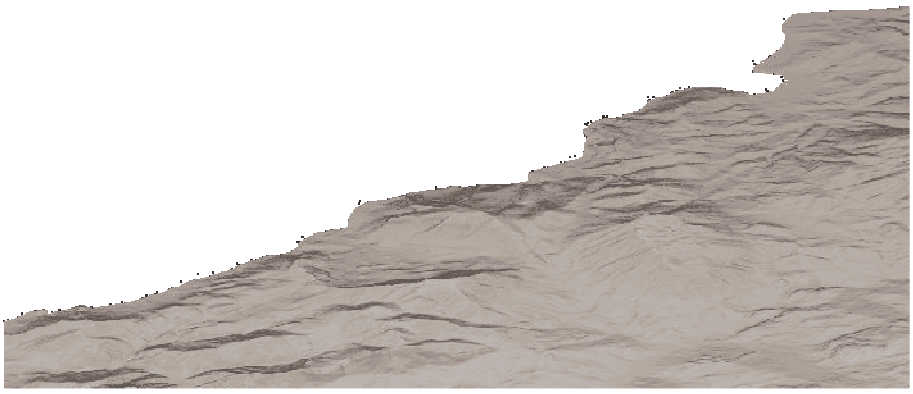

Figure 1 3D view of the interpolated DEM, as seen from ERS satellite.

Figure 2 Grey scale representation of the DEM in Fig.1.

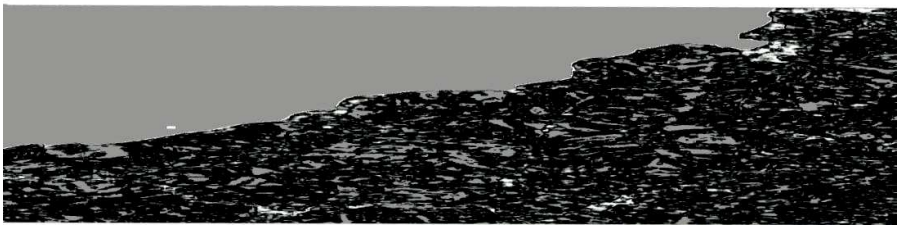

Figure 3 Map of the fractal dimension *D* of the considered DEM.

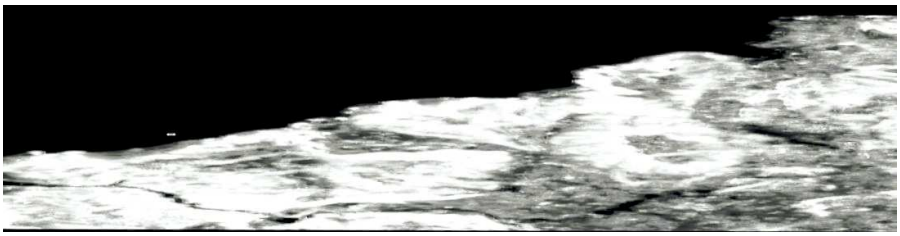

Figure 4 Map of the standard deviation for unitary increments *s* of the considered DEM.

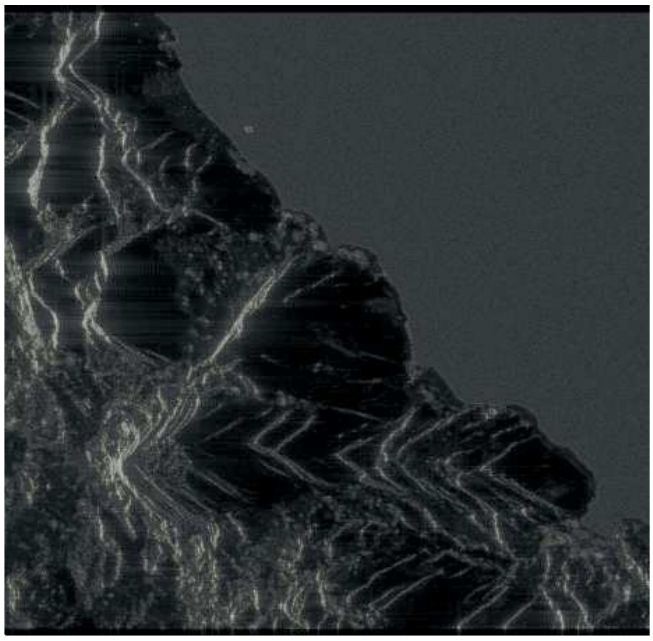

Figure 5 Simulated ERS amplitude image of Maratea (near range is on the left).

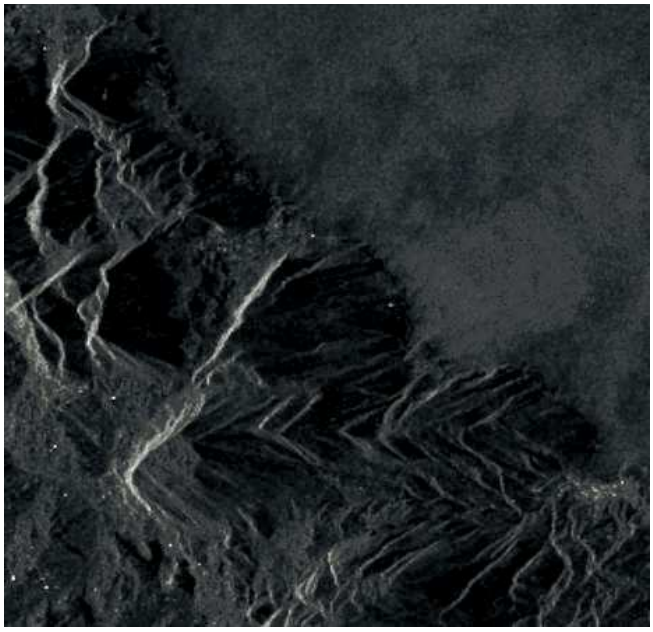

Figure 6 Actual ERS amplitude image of Maratea (near range is on the left).

3.1.2.2 Flooding

In the following, we present the potentiality of our framework applied to the monitoring of flooding. We modified the original DEM by creating a river's spate in the valley pinpointed by the black oval of Fig. 7. The mean difference between the pre- and post-crisis DEM in that area is about 30m. A close up of the flooded region before and after the disaster is presented in Fig. 8 and 9, respectively.

In order to appropriately simulate the presence of water in the flooded region, we modified the microscopic roughness and the dielectric parameters as well. As far as the microscopic fractal parameters are concerned, in the areas affected by the flooding we set H to a typical value for the water surface (H=0.75), and we set s to one half of the value in the pre-crisis scenario. As for the dielectric characterization, the area affected by the flooding is assumed to have a dielectric constant of $20\varepsilon_0$, and a conductivity of 1 S/m, which are typical values for extremely wet terrain; the surrounding area is assumed to have a dielectric constant of $4\varepsilon_0$ and a conductivity of 10^{-3} S/m, typical of terrains with low water content [13].

The SARAS simulated image corresponding to the post-crisis scenario is presented in Fig. 10. A visual comparison with Fig. 6 shows that the user can visually recognize the area hit by the flooding. Anyway, for actual cases a quantitative technique to identify the area involved in the phenomenon is required and its implementation is discussed in the following.

Therefore, the use of classical and fractal techniques is in order. A quantitative comparison is possible if a ground truth is available. Therefore, in order to define a reference map, we exploited the SARAS facilities of simulating the SAR image in absence of speckle. Such an approach allows the definition of the "ground truth" in the SAR image by differencing pre- and post-crisis intensity images in absence of speckle, and the creation of the reference mask of Fig. 11, where flooded regions are identified by white pixels.

Then, we tested the classical change detection technique based on the differencing between SAR intensity pre- and post-crisis images, obtaining a binary mask presented in Fig. 12. A visual comparison between Fig. 11 and 12 shows that the flooded area is well identified by the technique (we estimated that the hit rate is 97.2%), but this is paid with an excessive false alarm rate (11.2%), due to the fact that

the multiplicative random noise due to the speckle in correspondence of layover areas can significantly change from a realization to another. Note that, due to the peculiar distribution of the misclassified pixels, it is not trivial to improve the technique performance via classical post-processing algorithms.

Then, we implemented a change detection technique, based on the fractal framework presented in the previous sections. In particular, we used retrieved the pseudo-fractal parameters of pre- and post-crisis scenarios. In Fig. 13 we show a classification map obtained by the difference between the fractal dimensions of pre- and post-crisis scenes. Again, it is possible to identify the flooded area with a good hit rate (83%), but, again, the false alarm rate is extremely high (15.4%).

Anyway, by observing Fig. 12 and 13, we note that the distribution of misclassified pixels is completely different, due to the different causes that generate it. In fact, the image intensity difference is very sensitive to the signal magnitude changes, therefore most of the misclassified pixels are grouped in the layover areas (it is consistent with the fact that SAR signal correlation decreases in layover areas). Conversely, the fractal dimension is more sensitive to gradients of the signal, therefore most of the noise is gathered in correspondence of the grazing angle areas, where the differences between the side lobe of the layover areas create steep gradients. Above considerations suggest to combine the obtained results in order to get a significant improvement on the detection performances.

A simple multiplication of the obtained masks allows deleting most of the misclassified pixels, causing a strong reduction of the false alarm rate. Such a combined technique leads to a hit rate of 81.1%, with a false alarm rate reduced to 0.5%. A further low complexity processing can consist in a smoothing devoted to throw out isolated misclassified pixels, obtaining an improvement of the hit rate to 90.2%, paid with a false alarm rate raised to 0.6%, corresponding to the classification mask presented in Fig. 14. Figure 14 suggests that the residual false alarm error can be further reduced via simple post-processing algorithms.

Note that, by changing the thresholds used for the classification maps, the results can slightly change. Anyway, the choice of the thresholds is beyond the scope of this paper, it can be done in

accordance with the specific application and it does not change the essence of above presented results.

In addition, note that the *s* information was not used because, in this peculiar case, it does not bring a significant classification improvement. This is mainly due to the fact that, due to the particular topography, the *s* data and the image intensity information are strongly correlated.

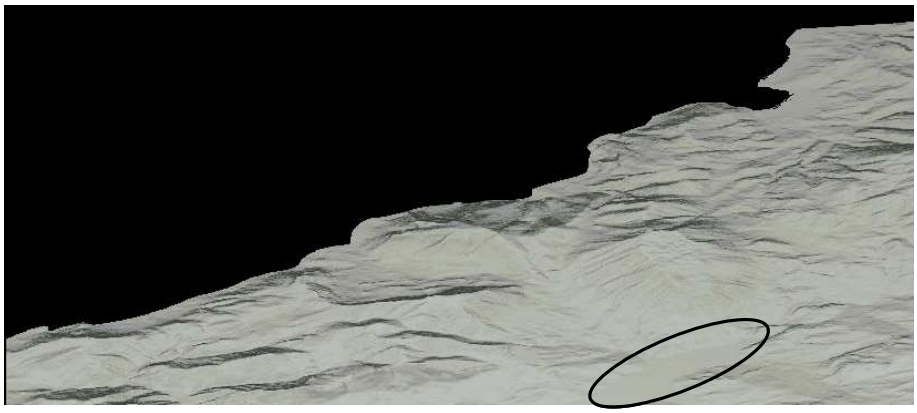

Figure 7 3D representation of the Maratea region after the flooding. Flooded area is marked in the black oval.

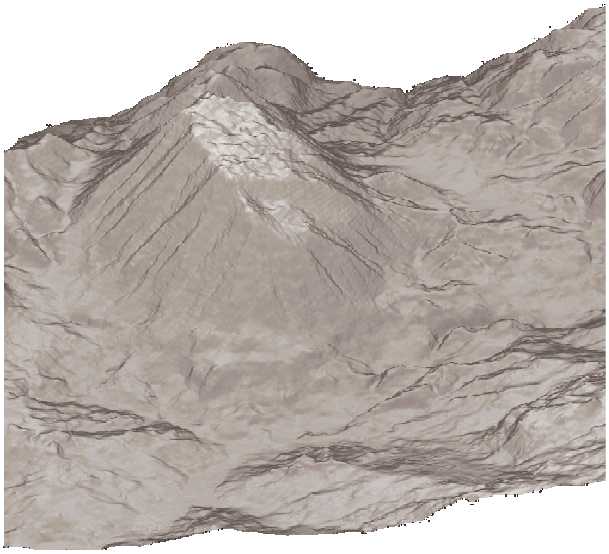

Figure 8 Close-up of the region of interest before the flooding.

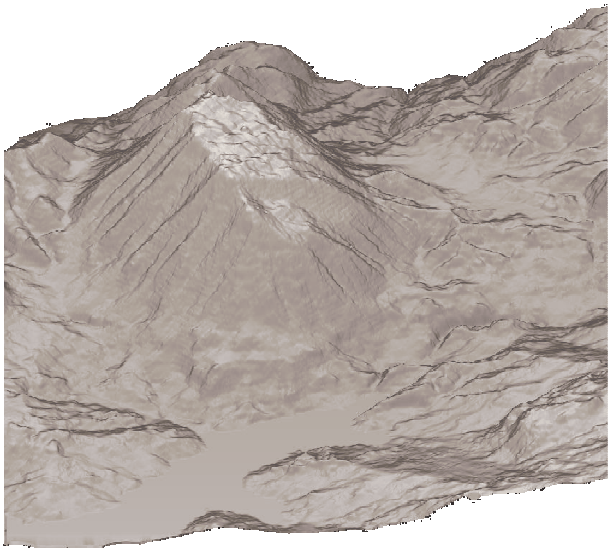

Figure 9 Close-up of the region of interest after the flooding.

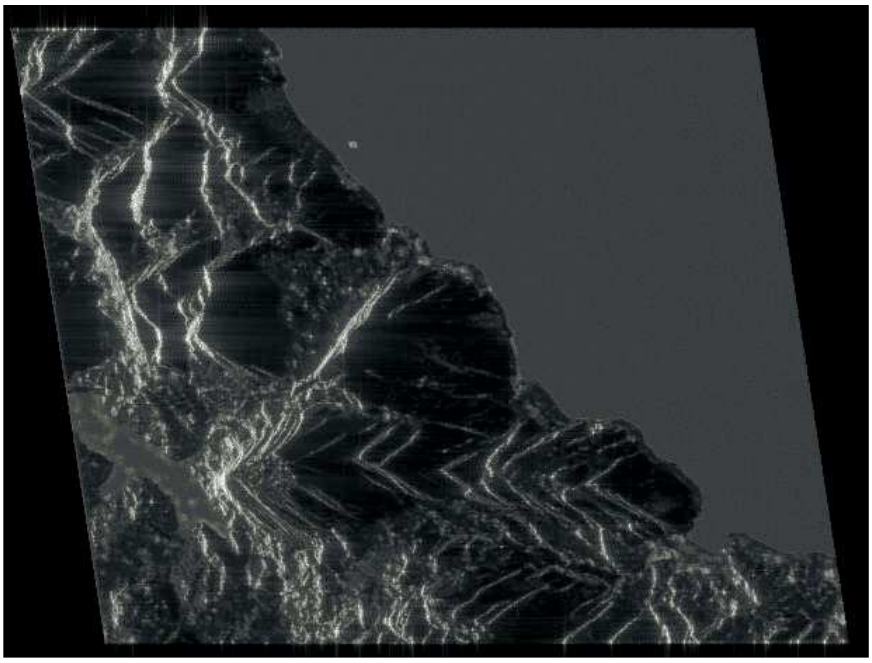

Figure 10 SAR simulation of the image relative to the post-crisis scenario as seen by the ERS-1 C band SAR sensor.

Figure 11 Reference classification map ("ground truth").

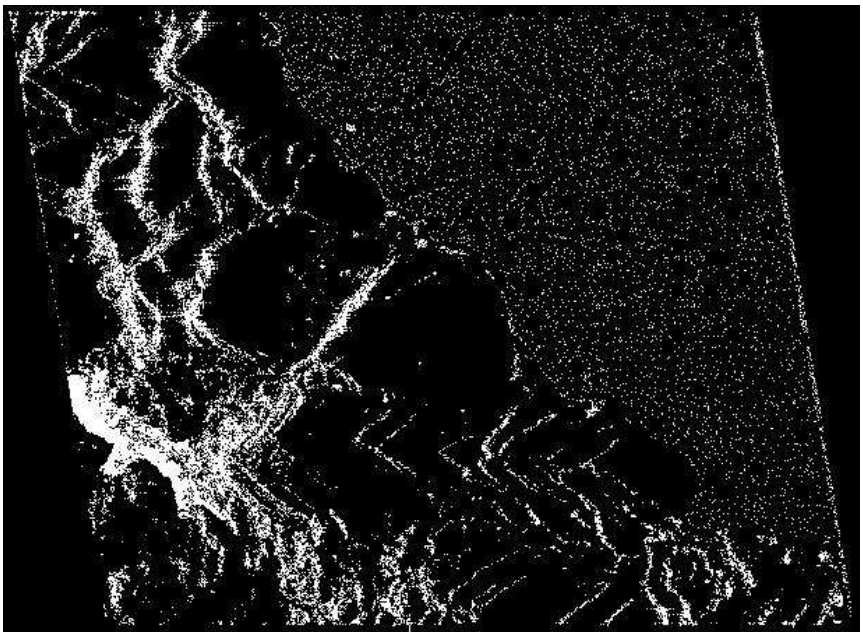

Figure 12 Classification map obtained by magnitude differencing.

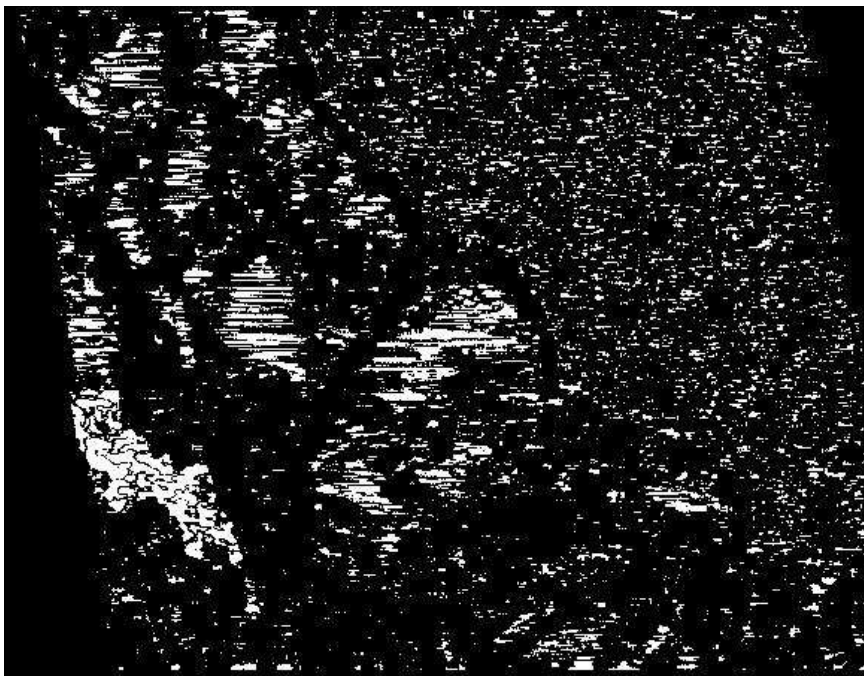

Figure 13 Classification map obtained by pseudo-fractal dimension differencing.

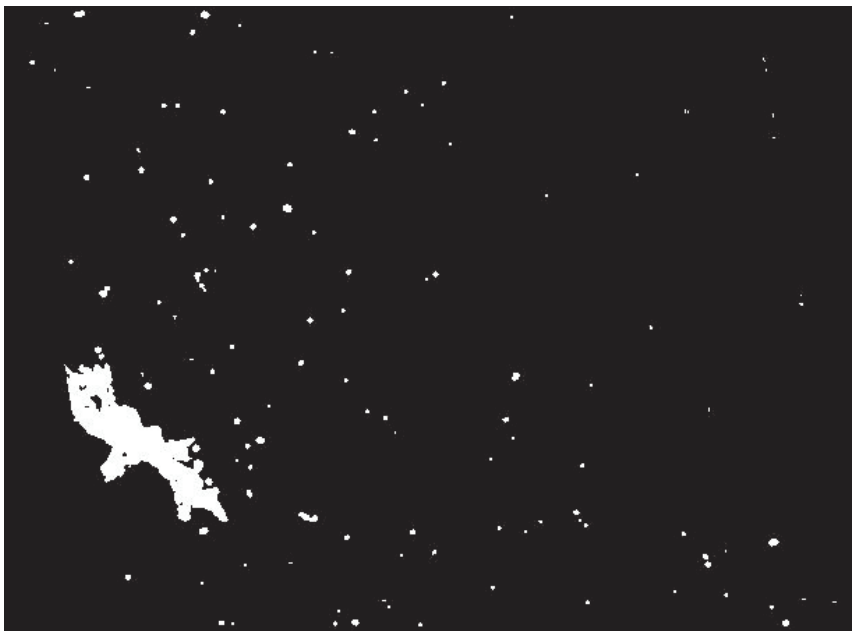

Figure 14 Classification map obtained with the combined technique.

3.1.2.3 Volcano eruption

In the following, we present a simulated volcano eruption scenario. We show the performance of our fractal approach for the identification of areas covered by the lava flows.

The first case is relevant to the Kilimanjaro volcano (2°S 36°E). We provided as input for the simulator the digital elevation model (DEM) of the zone, on a 90x90 m^2 grid. The DEM was interpolated via the fractal approach, in order to be in accordance with the ERS-1 acquisition geometry. In Fig. 15 we present a 3D representation of the DEM.

The simulation was performed according to the procedure presented in the previous Section. The simulated image is shown in Fig. 16 (near range is on the left). Such an image represents a reference for the situation, in absence of lava flows.

In order to assess the ability of the proposed technique, we simulated a lava eruption, by setting the simulation parameters of a given region to the typical values for the most common lava flows (AA and pahoehoe). However, to appropriately account for the presence of lava, we gave the region parameters the values defined in Table 1.

Two kinds of lava are defined: a smoother one, recalling the properties of the pahoehoe lava flows and a rougher one, recalling the properties of the AA lava flows. In Fig. 17 and 18 the two simulated SAR images are presented (near range is on the left).

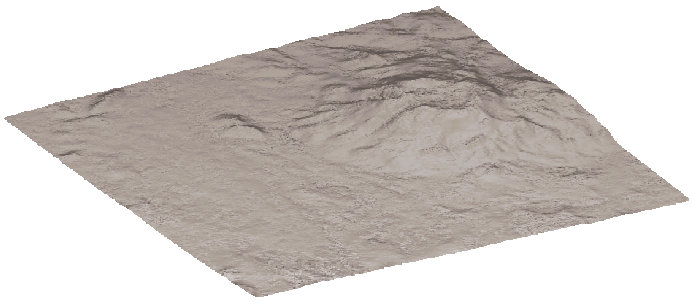

Figure 15 3D representation of the Kilimanjaro volcano area.

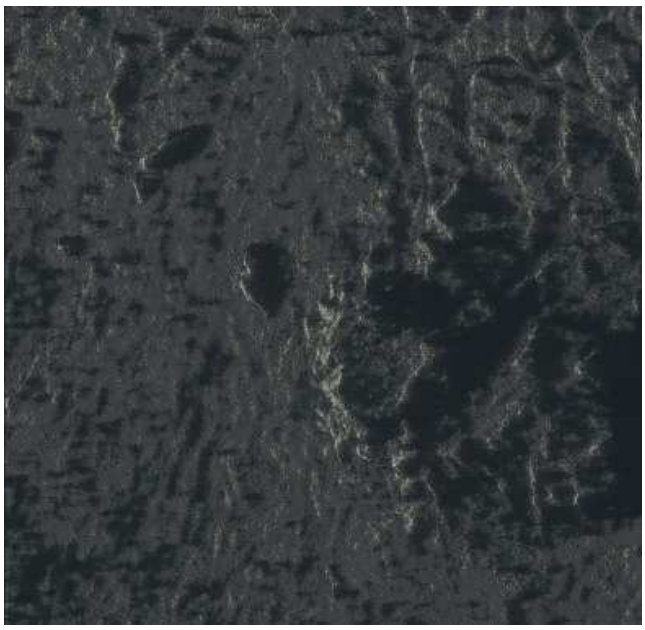

Figure 16 Simulated ERS-1 image of the Kilimanjaro area.

Table 1 Lava parameters.

Lava parameters	***AA***	***Pahoehoe***
Dielectric Constant	8	20
Conductivity [S/m]	0.01	1
Hurst coefficient	0.6	0.85
s [$m^{(1-H)}$]	0.1	0.2

On the obtained SAR images we applied the variogram method, obtaining the maps of the pseudo-fractal parameters of the two scenarios for change detection purposes. In this case, only one of the two independent parameters of the image, i.e. the *s* parameter, was used to identify the region covered by the lava. This is due to the fact that in our simulation we considered that the high scale profile is not changed by the lava flow.

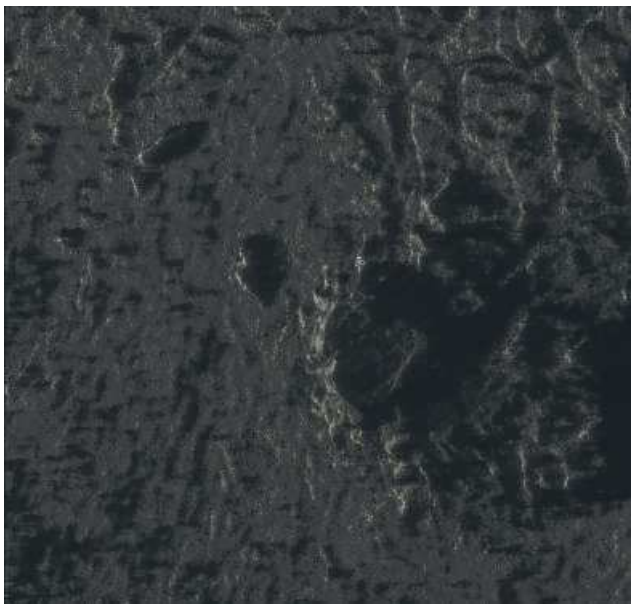

Figure 17 Simulated ERS-1 images of the Kilimanjaro area covered with pahoehoe lava.

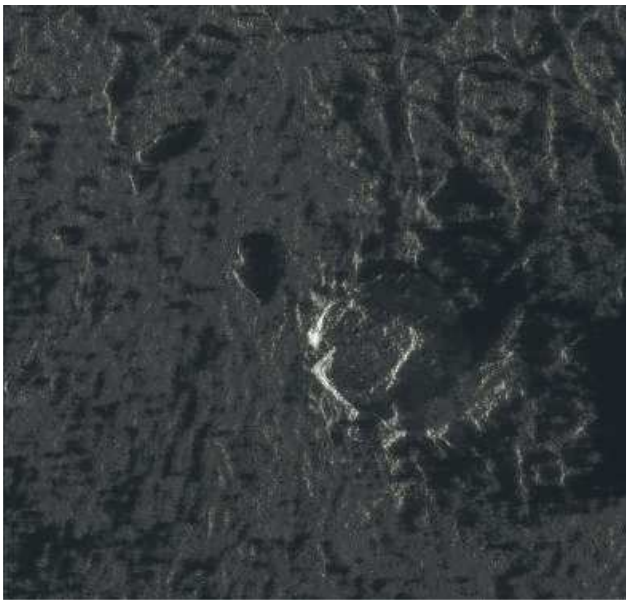

Figure 18 Simulated ERS-1 images of the Kilimanjaro area covered with aa lava.

Anyway, the presence of the lava in the scene significantly changes the surface characteristics of the area affected by the eruption at microscopic scale, and it is possible to exploit the sensitivity of the SAR return to the surface microscopic roughness. We simulated the volcano eruption by changing the microscopic parameters of the surface and this resulted, essentially, in a change of intensity of the image in the zone of interest.

In order to quantify the performance of the technique, a reference map can be generated, by simulating the SAR data in absence of speckle in the pre- and post-eruption cases. Their difference defines the “ground truth” for the case study. In Fig. 19 and 20 the ground truth and the map obtained with the proposed approach are shown.

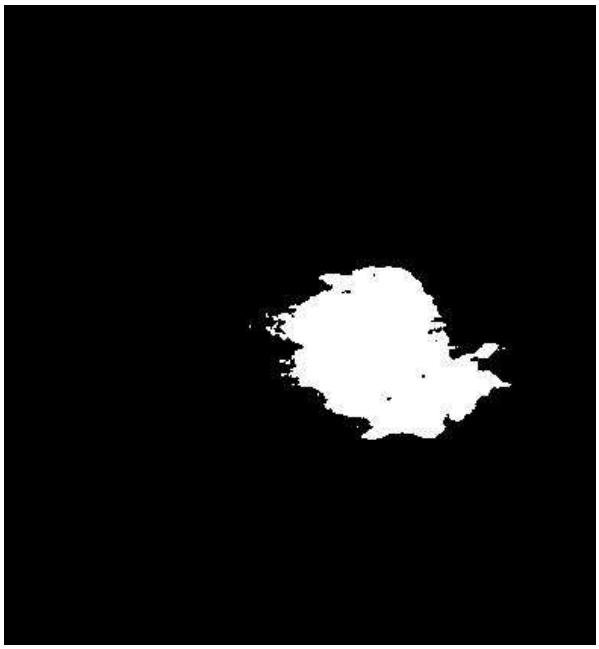

Figure 19 Ground truth map for the Kilimanjaro area.

Figure 20 Classification map obtained using the fractal technique.

If we compare the case of the flooding with that of the volcano eruptions, it is evident that in the former case the modification of the DEM at macroscopic scales determined a variation in the pseudo-fractal dimension of the image, resulting in information complementary with respect to that supplied by the *s* parameter. Essentially the pseudo-fractal dimension of the image shows a dependence on the fractal dimension of the imaged surface measured at the scales of SAR resolution rather than at wavelength scales. Anyway, this question will be fully clarified in the next chapter.

In the next section another kind of natural disaster is addressed: the problem of oil slicks in the sea, often related to ship illegal emissions. New instruments have been developed to support SAR simulation of these scenarios. The goal in this case is to identify the oil slicks and to discriminate them from look-alikes. Examples of possible post-processing techniques devoted to this goal and tested on our simulated images are also presented and commented.

3.2 Simulation of ocean scenes covered by oil slicks

It is widely known that oil slicks on the ocean surface can be observed in SAR images as dark spots. Nevertheless, the use of SAR data is still limited because dark areas in SAR images can be due to several phenomena, as lack of wind, natural oil, plankton, and so on [14], [15]. So far, this ambiguity limited the development of automatic oil detection procedure.

The work presented here is widely based on the SAR raw signal simulator of ocean scenes covered by oil slicks presented in Ref. [5]. Such a simulator relies on efficient models for the ocean description and for the electromagnetic field-ocean wave interaction. The ocean surface is described by means of a two scale model, including long (periods of about 100 meters), and short (periods of cm and mm) waves. In addition, intermediate scale waves are accounted for as an effect on the signal. A model based on the Marangoni theory accounts for the oil slick effect as well. The main limit of this simulator is that it was not possible to define a shape for the slicks.

In order to enlarge the range of applications of our simulator, we extended the simulator potentiality, providing the chance of generating slicks with arbitrary shapes. In particular, we focused our attention on the simulation of oil slicks with fractal shapes, because it is widely accepted that the fractal geometry is the most suitable instrument to generate natural profiles. In particular, we used the WM fractal function, presented in Chapter 2, to synthesize a fractal surface.

Once the oil slick was generated, we employed the obtained results as input for the SAR raw signal simulator. In particular, we simulated SAR images relative to fractal slicks as well as slicks with integer dimension, in order to emulate the characteristics of a ship emission.

One of the techniques often used to discriminate between natural and man-due slicks is the regularity of the contour. Therefore, we analyzed the obtained images, with the double goal of verifying the law of conservation of the fractal dimension, as well as the radiometric behavior of the oil covered area with respect to clean water.

3.2.1 Generation of oil slicks with arbitrary shapes

The estimation of the contour fractal dimension can be used in discriminating between natural and man-due slicks. Therefore, it can be interesting for oil detection purposes, to generate slicks with fractal shapes. In order to do it, the most appropriate function is the fBm. In the following a realization of an fBm process is synthesized by means of the Weiersrass-Mandelbrot function, as detailed in Chapter 2.

A cut of the WM function at fixed z levels provides a fractal curve which defines the region covered by the oil. As an example, in Fig. 21 we depict a slick obtained by a cut of a WM function with fractal dimension D_{WM} =2.35. The image was synthesized on a 3.99 x 19.9 m^2 spaced grid, in accordance with the ERS-1 acquisition geometry. The image pixel of Fig. 21 has a 19.9m x 19.9m (azimuth x range) dimension, in order to show the ground aspect of the slick. Therefore, such an image can be used as an input for the simulation of ERS-1 raw signals and images.

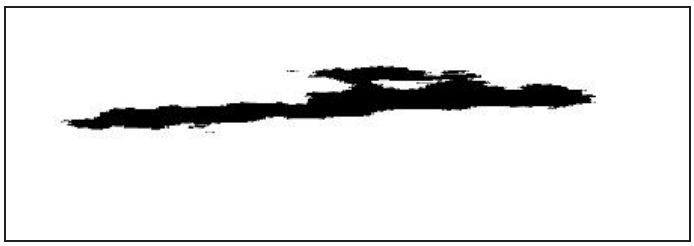

Figure 21 A fractal slick obtained as a cut of a WM function with fractal dimension D_{WM} =2.35.

In order to estimate the fractal dimension of the slick contour, we applied a box counting technique, and we obtained a fractal dimension Dc =1.38. It means that difference between the Hurst coefficient H of the contour (related to the fractal dimension D_c by the relation D_c =2-H) and that of the corresponding WM process is less than 4%. Similar results were found for different slicks.

In several cases, it is of interest to discriminate between natural and man-due slicks, by evaluating the regularity of the contour. Therefore, we generated slicks whose shapes recall the typical slicks spilled by the boats, by using the classical geometry. As an example,

in Fig. 22 we present the shape of a slick, obtained as a brunch of a spiral function.

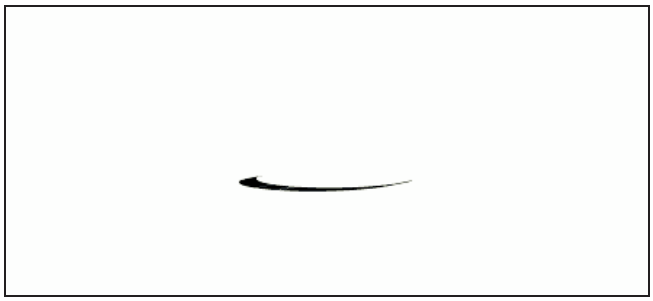

Figure 22 A slick obtained as a branch of a spiral.

As we stated in Chapter 2, the oil influence on the sea surface is accounted for via the Marangoni theory, as a damping of the ocean spectrum. The intensity of the damping depends on the oil properties and it is presents a resonant behavior. Therefore, the best sensor for oil detection depends also by the oil resonant frequency. As an example, the Oleyl Alchool, which is here considered as case study, presents a resonance around spatial frequency that corresponds to the C-band.

The C-band ERS-1 SAR image relevant to the oil slick whose shape was shown in Fig. 21 is obtained from the simulated raw signal via standard processing and presented in Fig. 23. The image is averaged with a 1 x 4 multi-look, so that its resolution in azimuth – slant range is 19.9 x 7.9 m^2, which corresponds to an azimuth – ground range approximately square pixel (19.9 x 19.9 m^2).

Figure 23 Simulated ERS-1 SAR image relative to the slick synthesized in Fig. 21. The near range is on the left.

In order to show the image dependence on the carrier frequency we simulated the SAR image signal relative to the previous scene,

acquired by the SIR-C sensor, which works at L band. In Fig. 24 the corresponding SAR image is shown. The image is averaged with a 1 x 4 multi-look, so that its resolution in azimuth – slant range is 18.3 x 13.3 m^2, which corresponds to an azimuth – ground range approximately square pixel (17.7 x 18.3 m^2). As expected, the image damping is strongly reduced, because the working frequency is in an area where the spectral damping is lower.

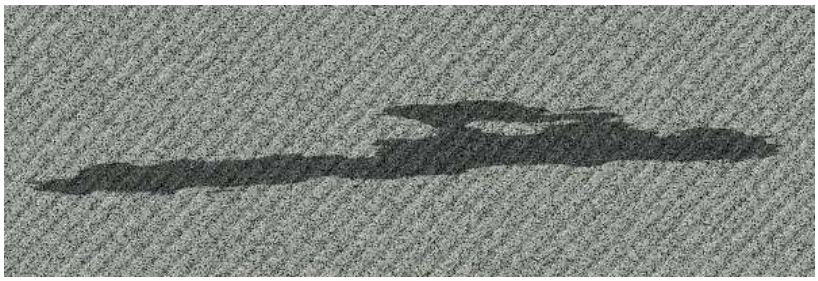

Figure 24 Simulated SIR-C SAR image relative to the slick synthesized in Fig. 21. The near range is on the left.

In Fig 25 we present also the SAR simulation relevant to a slick with the classical contour presented in Fig. 22. The slick properties were chosen with the goal of reproducing the geometrical characteristics of a slick spilled by a boat.

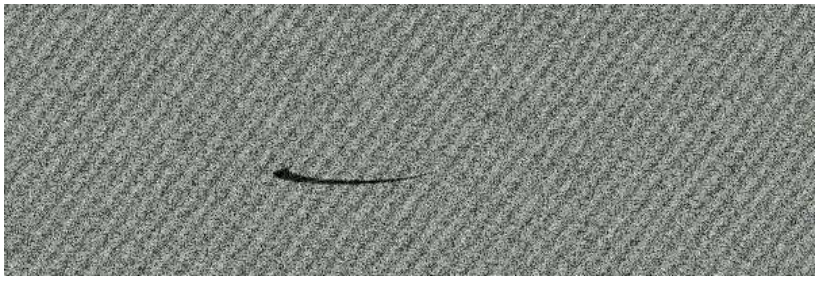

Figure 25 Simulated SAR image reproducing a boat emission. The near range is on the left.

The introduced ability of the simulator can also be exploited to account for a typical ambiguity problem, related with the lack of wind. In fact, it is now possible to generate arbitrary shaped regions where the wind intensity is supposed to be reduced with respect to the background. As an example, in Fig. 26 we show a simulated ERS-1

image with the contemporary presence of an oil slick and a lack of wind.

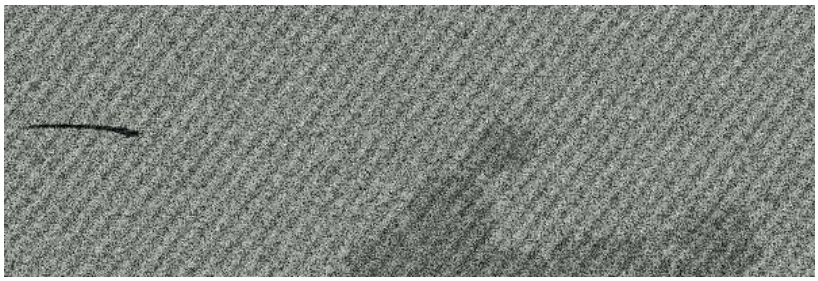

Figure 26 Simulated SAR image relative to a boat emission (on the left), and a lack of wind (on the right). The near range is on the left.

3.2.2 Image analysis

The presented simulator can be intensively exploited to generate a set of images that can be used to improve the comprehension of the image characteristics and for training of detection techniques. In addition, the ability of simulating lack of wind and oil slicks gives the opportunity of facing the problem of the ambiguity solution as well.

In the following, we present some examples on how simulated images can be a support for developing SAR techniques. In particular we focus our attention on the estimation of the slick contour fractal dimension, which can be a classification criterion, and on radiometric analysis.

3.2.2.1 Fractal technique

Let us consider the SAR images relative to the slicks generated in the previous section and the possible estimation of the fractal dimension of their contour. The evaluation of the fractal dimension is possible if the pixels belonging to the slick are identified. This operation can be performed by defining a threshold image intensity value. Of course such an approach is limited by the speckle noise that makes ambiguous the pixel classification.

Anyway, the combined use of morphological operators allows the extraction of the slick contour. As an example, in Fig. 27 we show the contour extracted by the SAR image presented in Fig. 24.

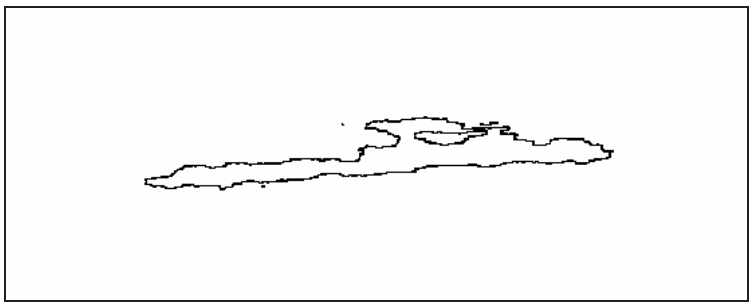

Figure 27 Contour extracted by the SAR image of Fig. 24.

The contour fractal dimension was then evaluated via a box counting algorithm, obtaining a value D_c =1.3. As expected, the fractal dimension is similar to the slick mask, slightly reduced by the morphological operations required to limit the speckle noise effect. Similar results were obtained for fractal slicks with different fractal dimension.

The evaluation of the fractal dimension was also performed on the image presented in Fig. 25. Note that the extension of the slick is much more limited, therefore, the extraction of the contour and the evaluation of the fractal dimension can suffer for reliability problems. The obtained fractal dimension value D_c =0.9 confirms that the slick contour does not hold fractal property. It appears clear that the evaluation of the slick contour fractal dimension can be a technique for ambiguity removal.

3.2.2.2 Radiometric techniques

The slick classification is often addressed via the combined use of the contour fractal dimension retrieving and techniques based on the analysis of the SAR image radiometric properties. The presented simulator provides a huge amount of data for the developing and training of radiometric techniques as well. In the following, we recall an innovative technique for the discrimination between oil slicks and lack of wind, argued by theoretical considerations, and verified with the use of simulated data [5].

As stated in Chapter 2, the intensity of the electromagnetic return scattered by a portion of the sea surface is proportional to the ocean spectrum at frequencies sampled by the Bragg relation. The oil

presence damps the ocean spectrum and it changes the higher order statistics, at variance of a lack of wind, which causes a rigid damping of the ocean spectrum.

Therefore, the estimation of the normalized intensity moments (introduced in Chapter 1) on several simulated SAR images led to verify that the higher order moments in areas covered by oil are modified with respect to the clean water and to areas where a lack of wind is present. The main limit of this technique was related to the fact that in actual cases the slick dimension often does not provide a sufficient population for evaluating reliable statistics. Anyway, the extension of the simulator presented in this paper allows the generation of a huge set of SAR images, devoted to quantitatively face the study of the limits of the technique, in terms of the slick geometrical characteristics.

References

[1] L. Hess, J. M. Melack, S. Filoso, and Y. Wang, “Delineation of Inundated Area and Vegetation Along the Amazon Floodplain with the SIR-C Synthetic Aperture Radar”, *IEEE Trans. Geosci. Remote Sens.*, Vol. 33, 896-904, Jul. 1995.

[2] M. Gianinetto, P. Villa, and G. Lechi, “Postflood Damage Evaluation Using Landsat TM and ETM+ Data Integrated With DEM”, *IEEE Trans. Geosci. Remote Sensing*, Vol. 44, 236-243, Jan. 2006.

[3] P. Lundgren, P. Berardino, M. Coltelli, G. Fornaro, R. Lanari, G. Puglisi, E. Sansosti and M. Tesauro, “Coupled Magma Chamber Inflation and Sector Collapse Slip Observed with Synthetic Radar Interferometry on Mt. Etna”, *Journal of Geophysical Research*, 108, n. B5, 2247-2262, 2003.

[4] F. Colesanti, A. Ferretti, C. Prati, and F. Rocca, “Monitoring Landslides and Tectonic Motions with the Permanent Scatterers Technique”, *Engineering Geology*, 68, 3 –14, 2003.

[5] G. Franceschetti, A. Iodice, D. Riccio, G. Ruello, and R. Siviero, "SAR Raw Signal Simulation of Oil Slicks in Ocean Environments," *IEEE Trans. Geosci Remote Sens.*, vol. 40, no. 9, Sep. 2002.

[6] P. M. Barbosa, J.-M. Grégoire and J. M. C. Pereira, "An Algorithm for Extracting Burned Areas from Time Series of AVHRR GAC Data Applied at a Continental Scale", *Remote Sensing of Environment*, 69:253-263, 1999.

[7] B.B. Mandelbrot, *The Fractal Geometry of Nature*, W.H.Freeman & C., New York, USA, 1983.

[8] G. Franceschetti, D. Riccio, *Scattering, Natural Surfaces and Fractals*. Academic Press, Burlington (MA), USA, 2007.

[9] E. Rignot and J. van Zyl, "Change Detection Techniques for ERS-1 SAR Data", *IEEE Trans. Geosci. Remote Sens.*,vol. 31, no. 4, pp.896-906, Jul. 1993.

[10] M. Carlotto, "Detection and Analysis of change in Remotely Sensed Imagery with Application to Wide Area Surveillance", *IEEE Trans. Image Process.*, vol.6, no.1, pp.189-202, Jan. 1997.

[11] N. Yocoya, K. Yamamoto, N. Funakubo, "Fractal-based Analysis and Interpolation of 3D Natural Surface Shapes and Their Application to Terrain Modeling", *Computer Vision, Graphics, and Image Processing*, vol.46, pp.284-302, 1989.

[12] G. Franceschetti, M. Migliaccio, D. Riccio, "SAR Raw Signal Simulation of Actual Scenes Described in Terms of Sparse Input Data", *IEEE Trans. Geosci. Remote Sens.*, GE-32, 1160-1169, Nov.1994.

[13] F. T. Ulaby, R. K. Moore and A. K. Fung, *Microwave Remote Sensing: Active and Passive*, Reading, MA: Addison-Wesley, 1982.

[14] J. C. Scott, "Ocean Surface Slicks - Pollution, Productivity, Climate and Life Saving", *Proc. IGARSS '99*, Hamburg, 1999.

[15] M. Gade, W. Alpers, H. Huhnerfuss, H. Masuko and T. Kobauashi, "Imaging of Biogenic and Anthropogenic Ocean Surface Films by the Multifrequency/Multipolarization SIR-C/X-SAR", *J. Geophys. Res.*, vol. 18, pp. 851-866, 1988.

Chapter 4

Microwave Imaging

In several geophysical applications the retrieval of significant parameters of an observed surface from radar data would be of key importance. However, this is often limited by the lack of reliable mathematical models able to quantitatively support the retrieving of value-added information on the scene under survey.

In this chapter we provide an answer to the question raised in the previous chapter on whether the microwave image relevant to a fractal surface is fractal or not. In particular, the characteristics of images relevant to a fractal profile are here investigated.

In our study we follow a twofold approach: on one side, we develop a rigorous analytical formulation for the problem assuming a particular class of small slope profiles; on the other side, we present an experimental setup able to deal with the general case. As for the analytical approach, we show that the signal backscattered from a fractal profile modeled as an fBm stochastic process is strictly related to the associated fractional Gaussian noise (fGn) process when a small slope regime for the observed profile can be assumed: in this case we are able to compute in closed form the structure function and the power density spectrum of the signal. Our results are obtained introducing an fBm smoothed process, which is justified by the low-pass filtering introduced by the sensor impulse response function.

The experimental framework is based on sound direct models allowing the synthesis of the profile, the evaluation of the backscattered signal via fractal scattering models and the estimation of the power density spectra of interest. Note that this is the only fully fractal approach found in the open literature on this subject, i.e. presenting a coherent choice of the considered geometric and electromagnetic models. Anyway, the proposed approach can be used also to analyze the case of heuristic scattering models, as will be clarified in the following.

4.1 Imaging of one-dimensional fractal profiles

Due to the outstanding development of the remote sensing instruments and processing techniques occurred in the last decades, a huge amount of data relevant to any part of the globe is now being available. A new generation of sensors is providing a great amount of data that could increase the possibility to extract very valuable information. As a matter of fact, the possibility to obtain value added information from satellite data can be of great relevance for agriculture [1], rural and urban planning [2], disaster monitoring and assessment [3], and so forth. In particular, as far as geophysical applications are under concern, retrieving from remote sensing data significant parameters relevant to an observed surface is of open issue of key importance.

In this section we provide a description of the imaging process that can be used as a support to feature extraction from radar data. Among different remote sensors, we focus on the imaging ones, which generate synoptic views of the area under survey thus providing punctual as well as distributed (textural) information on the remote sensed area. Texture on remotely sensed images is related to morphological and geological features, land use and social organization of the observed scene. By employing supervised techniques, an expert user can distinguish human signatures, which are well described within the classical geometry, from natural features, that conversely are better described by means of fractal geometry.

Indeed, fractal geometry proved to be the most appropriate mathematical instrument to describe the self-similarity and irregularity of natural scenes, by means of few independent parameters [4]-[6]. Among fractal models, the fractional Brownian model (fBm) stochastic model is maybe the better choice for the description of this family of surfaces. However, fBm mathematical surfaces present a major disadvantage: they are strictly not differentiable. Hence, as we have seen in Chapter 2, we have to introduce physical fractals and to effectively define the derivative of this class of surfaces. In this section, we focus our attention on the (Euclidean) one-dimensional problem assuming an fBm geometrical model for the observed profile: this simplified environment allows the presentation of our innovative

approach, emphasizing the somehow unexpected results without hampering the mathematical issues. As a matter of fact, the extension to the (Euclidean) two-dimensional case is not straightforward: isotropy issues on fractal surfaces are to be taken into account and the mathematical approach becomes quite involved; the first steps toward the extension to the two-dimensional case are presented in the next section.

The study of the physical phenomena occurring in the remote sensing of fractal surfaces is, obviously, of key importance for the retrieving of value added information from the images. As a matter of fact, we are interested not only in the estimation of significant parameters of the imaged surface, but also in achieving a better understanding of this kind of images avoiding the application of improper image processing techniques. In fact, the radar images are proposed under the form of a great variety of products, with different degrees and types of elaboration: actually, this can damage the information content of the original image of natural scenes. Hence, the interest is focused not only on the efficient retrieving of the fractal parameters, but also to the development of new, information-preserving image processing techniques.

In the open literature the works addressing these subjects are sparse and not always accurate enough to provide reliable results. Most of the available works refer to the pioneer papers due to Pentland [7]-[8], who studied the optical imaging of fBm surfaces, assuming a Lambertian scattering behavior. However, the choice of the electromagnetic scattering model used to compute the field backscattered from a random rough surface should be definitely dependent on the geometric model used in describing the surface itself. As we argued in Chapter 2, has been demonstrated that the use of adequate scattering models strongly improves the accuracy in the evaluation of the signal backscattered from fractal surfaces. Hence in this work use is made of appropriate fractal geometric and electromagnetic models: to the best of our knowledge, this is the only work presenting a completely fractal framework for this subject. In particular, we present here a twofold approach providing, on one side, an analytical closed form solution to the imaging problem in the case a small slope regime for the observed profile can be assumed, and, on

the other side, a sound model-based, experimental setup to study the general case.

In the following sub-section we compare our work with existing ones and provide the fundamentals of the problem.

4.1.1 Pentland model

In Refs. [7] and [8], Pentland copes with the problem of the imaging of fBm surfaces. His approach is based on a linear approximation of the image intensity as a function of the partial derivatives of the surface: the underlying hypothesis is that the slopes of the observed surface can be assumed to be small. However, it is possible to split his work into two parts: 1) the assumption of a particular irradiation behavior (i.e., the Lambertian one) for the considered surface; 2) the evaluation of the power density spectrum of the image, in the hypothesis of validity of the aforementioned linear approximation.

With regard to the former point, we note that the considered scattering behavior is not always adequate to describe the electromagnetic scattering from the considered surface: for instance, theoretical and experimental results show that at microwave frequencies the scattering from natural surfaces is definitely not Lambertian-like [9]-[10]. As argued in the previous chapters, an arbitrary choice of the scattering radiation diagram, regardless of the considered surface model, is a common misbehavior: most of the works available in literature and dealing with this subject use some heuristic function to describe the scattering from an fBm surface [11]-[12]. As a matter of fact, each surface model calls for an appropriate scattering method and it has been shown in Chapter 2 that, if we assume an fBm model for the observed surface, we have to use appropriate fractal-based scattering methods for the evaluation of the scattering. The evaluation of a quantitative condition establishing the possibility to assume the small slope regime of the profile in term of its fractal parameters with respect to this fractal scattering models is a key future development of this thesis work: we note, by the way, that this issue is also related to the accurate definition of validity limits for the scattering models themselves, which is itself a delicate point as we have seen in Chapter 2.

With regard Pentland's evaluation of the power density spectrum of the image, some important remarks are in order. The expression given by Pentland for the image intensity can be written as follows:

$$i(x,y) \cong a_0 + a_1 p(x,y) + a_2 q(x,y) \tag{4.1}$$

where $p(x,y)$ and $q(x,y)$ are the partial derivatives of the surface and $a_{0,1,2}$ are the coefficients of the Mac Laurin series expansion of $i(x,y)$ for small values of $p(x,y)$ and $q(x,y)$. The main problem of (4.1) is that $p(x,y)$ and $q(x,y)$ do not exist anywhere for fractal surfaces. To circumvent this problem, in his analysis Pentland formally works with the partial derivatives of the surface, stating, in a note, that, due to the non-differentiability of the mathematical fBm, he considers a sufficiently smoothed approximation of the sensed surface that allows the existence of the partial derivatives. However, in the following of his work he keeps working using the formal definition of derivative, i.e. without introducing a smoothed process. In remote sensing applications, but, more in general, in all engineering matters, the formal use of the smoothed process is not only desirable but necessary. As a matter of fact, the features of the scene relevant to spatial scales much smaller than the wavelength one do not contribute to the scattering phenomenon: in this sense, the electromagnetic incident field acts as a low-pass filter on the surface. Furthermore, scales smaller and larger than the resolution one contribute in different ways to the formation of the image: however, this crucial issue deserve the maximum attention and is, accordingly, fully clarified in the following.

4.1.2 The small slope analytical model

In this sub-section we provide the details of the developed analytical model. First of all the fGn process is introduced and novel results on its spectrum and structure function are presented. Then, starting from these results, the proposed imaging model is described.

4.1.2.1 Fractional Gaussian noise (fGn)

In Chapter 2, we presented the fBm two-dimensional process. In this section we are interested to one-dimensional profiles: after adapting the variables to meet with the one-dimensional case, the expressions of the structure function and of the power density spectrum are the same with respect to the two-dimensional case:

$$V(\tau) = s^2 \tau^{2H} \tag{4.2}$$

$$S(k) = S_o k^{-\alpha} \tag{4.3}$$

Obviously some of the involved parameters change their values as follows:

$$D = 2 - H \tag{4.4}$$

$$\alpha = 1 + 2H = 5 - 2D \tag{4.5}$$

$$S_0 = s^2 \frac{\pi H}{\cos(\pi H)} \frac{1}{\Gamma(1-2H)}. \tag{4.6}$$

We discussed how properly employing Pentland approach requires an expression for the derivative of the surface. The fractional Gaussian noise (fGn) is defined as the derivative process of the fBm: for the particular case of H = 0.5, we obtain the derivative of the Brownian motion, i.e. a white Gaussian noise [13]. The mathematical fBm is strictly non-differentiable, implying that its derivative process has to be handled with care. The most elementary method to deal with the fBm lack of derivative is to smooth the original process with an adequate kernel, discarding the high frequency effects responsible for the non-differentiability of the fBm. Hence, starting from the standard fBm process $z(x)$, we build the random function $z_\varphi(x)$:

$$z_\varphi(x) = \int_{-\infty}^{\infty} z(x')\varphi(x - x')dx' \tag{4.7}$$

where φ is the test function. In particular, by assuming $\varphi \in C_0^\infty\left(\overline{\Omega}\right)$, with $\Omega \subseteq R$ an open set, the expression (4.7) can be seen as a distribution [14], and the k-th derivatives of z_φ can be rigorously computed as:

$$z_\varphi^{(k)}(x) = (-1)^k \int_{-\infty}^{\infty} z(x')\varphi^{(k)}(x-x')dx' \tag{4.8}$$

However, for our purposes, an infinitely differentiable kernel is not necessary; hence, for the sake of simplicity, we select $\varepsilon > 0$ and set the test function as follows:

$$\varphi(x) = \begin{cases} \dfrac{1}{\varepsilon} & \text{if } x \in [0,\varepsilon] \\ 0 & \text{otherwise} \end{cases} \tag{4.9}$$

Substituting (4.9) in (4.8) and computing the first derivative of the process, we obtain:

$$z'(x;\varepsilon) = -\int_{-\infty}^{\infty} z(x')\varphi'(x-x')dx' = -\varepsilon^{-1}\int_{-\infty}^{\infty} z(x')\left[\delta(x-x') - \delta(x+\varepsilon-x')\right]dx' \tag{4.10}$$

δ being the *Dirac delta* distribution. Therefore we can easily compute the derivative as:

$$z'(x;\varepsilon) = \varepsilon^{-1}\left[z(x+\varepsilon) - z(x)\right] \tag{4.11}$$

In this way the derivative of the smoothed process can be seen as a finite difference, presenting some interesting properties. Note that in this case we can easily evaluate the autocorrelation function as the correlation between two increments of the original fBm process, obtaining a stationary non isotropic Gaussian process with $\mu = 0$ and $\sigma = s\varepsilon^{H-1}$. Its autocorrelation function can be computed as follows:

$$R_{z'}(\tau;\varepsilon)=\langle z'(x;\varepsilon)z'(x+\tau;\varepsilon)\rangle=\langle (z(x+\varepsilon)-z(x))(z(x+\tau+\varepsilon)-z(x+\tau))\rangle$$
$$=\langle z(x+\varepsilon)z(x+\tau+\varepsilon)-z(x+\varepsilon)z(x+\tau)-z(x)z(x+\tau+\varepsilon)+z(x)z(x+\tau)\rangle \quad (4.12)$$

The four terms in the brackets can be evaluated using the expression of the original surface autocorrelation, obtaining:

$$R_{z'}(\tau;\varepsilon)=\frac{1}{2}s^2\varepsilon^{2H-2}\left[\left(\frac{|\tau|}{\varepsilon}+1\right)^{2H}-2\left|\frac{\tau}{\varepsilon}\right|^{2H}+\left|\frac{|\tau|}{\varepsilon}-1\right|^{2H}\right] \quad (4.13)$$

If $\frac{\tau}{\varepsilon}\gg 1$, expanding to the second order the first and the last term in the square brackets of (4.13), we obtain:

$$R_{z'}(\tau)\cong s^2H(2H-1)|\tau|^{2H-2} \quad (4.14)$$

For a stationary isotropic stochastic process the structure function can be derived from the autocorrelation function, obtaining for the case of interest the following expression:

$$V_{z'}(\tau;\varepsilon)=s^2\varepsilon^{2H-2}\left[2-\left(\frac{|\tau|}{\varepsilon}+1\right)^{2H}+2\left|\frac{\tau}{\varepsilon}\right|^{2H}-\left|\frac{|\tau|}{\varepsilon}-1\right|^{2H}\right] \quad (4.15)$$

and in the limit $\frac{\tau}{\varepsilon}\gg 1$

$$V_{z'}(\tau;\varepsilon)=2s^2\left[\varepsilon^{2H-2}-H(2H-1)|\tau|^{2H-2}\right] \quad (4.16)$$

Being $z'(x;\varepsilon)$ a stationary process, we can evaluate its spectrum by employing the Wiener-Kintchine theorem. In particular, we can express the power spectrum of $z'(x;\varepsilon)$ as

$$S_{z'}(k;\varepsilon)=\frac{1}{2}s^2\varepsilon^{2H-2}\int_{-\infty}^{\infty}\left[\left(\frac{|\tau|}{\varepsilon}+1\right)^{2H}-2\left|\frac{\tau}{\varepsilon}\right|^{2H}+\left|\frac{|\tau|}{\varepsilon}-1\right|^{2H}\right]e^{-ik\tau}d\tau \tag{4.17}$$

It is very informative to evaluate this spectrum in closed-form. However, this spectrum does not follow within the class of functions whose Fourier Transform is known in $L^2(\Omega)$. To evaluate this spectrum we propose to resort to generalized Fourier transforms; in particular, we compute the transform of the second term of (4.17) as

$$\int_{-\infty}^{\infty}\left|\frac{\tau}{\varepsilon}\right|^{2H}e^{-ik\tau}d\tau=-\varepsilon^{-2H}\,2\Gamma(1+2H)\sin(\pi H)\frac{1}{|k|^{1+2H}} \tag{4.18}$$

Using basic Fourier transform properties (that are also valid for the generalized transforms), we can write the first and third term of (4.17) as follows:

$$\int_{-\infty}^{\infty}\left|\frac{\tau}{\varepsilon}\pm1\right|^{2H}e^{-ik\tau}d\tau=\varepsilon^{-2H}\int_{-\infty}^{\infty}|\tau\pm\varepsilon|^{2H}e^{-ik\tau}d\tau=\varepsilon^{-2H}e^{\pm ik\varepsilon}\int_{-\infty}^{\infty}|\tau|^{2H}e^{-ik\tau}d\tau \tag{4.19}$$

By exploiting the result in (4.18), we can evaluate the integrals in (4.19) thus obtaining:

$$\int_{-\infty}^{\infty}\left|\frac{\tau}{\varepsilon}\pm1\right|^{2H}e^{-ik\tau}d\tau=-\varepsilon^{-2H}e^{\pm ik\varepsilon}\,2\Gamma(1+2H)\sin(\pi H)\frac{1}{|k|^{1+2H}} \tag{4.20}$$

Substituting the results in (4.20) and (4.18) into Eq. (4.17) and using the Eulero formula, we get the final result, i.e. the power density spectrum of the derivative process of the smoothed surface profile:

$$S_{z'}(k;\varepsilon)=2s^2\varepsilon^{-2}\Gamma(1+2H)\sin(\pi H)\left(1-\cos(k\varepsilon)\right)\frac{1}{|k|^{1+2H}} \tag{4.21}$$

In the limit of $k\varepsilon << 2\pi$, Eq. (4.21) takes the relevant form:

$$S_{z'}(k) = s^2\Gamma(1+2H)\sin(\pi H)\frac{1}{|k|^{2H-1}} \tag{4.22}$$

From equations (4.21) and (4.22) we can draw some important conclusions. First of all, looking to the spectral exponent in Eq. (4.22) it's evident that the fGn can be seen as a fractal with $H \in [-1,0]$, which is in agreement with previous observations made by Voss [15]; anyway, as a matter of fact, this definition, although tempting, is not an accurate one, because if $H \notin [0,1]$ an associated stochastic process whose fractal dimension is $D = 2 - H$ exists with zero probability. In fact, we can draw the conclusion that fGn is a stationary Gaussian self-affine process, but it is not a fractal one, in the sense that we cannot define a Hausdorff-Besicovitch fractional dimension for this class of processes. Furthermore, looking at Eq. (4.21), we can note that the fGn shows a spectral power law behavior only asymptotically, for sufficiently low frequencies. In fact, as soon as the spatial frequency approaches the value $1/\varepsilon$, the oscillating behavior begins to dominate, being the first null for $k=2\pi/\varepsilon$.

However, though not fractal, the fGn process somehow inherits the fractal parameters of the original fBm process: starting from the results presented above, we can develop a novel imaging model and provide some hints on the retrieving of these parameters.

4.1.2.2 The imaging model

Here we present a model for the imaging process along with its application to fractal profiles. According to Pentland model, the imaging procedure can be seen as a block whose input is the surface profile, and whose output is the radar intensity image which is proportional, to the first order, to the derivative of the surface profile. Hence, in the following a closed form analytical solution for the small slope regime is obtained and investigated in detail.

First of all we note that an analytical study of radar imaging of fractal surfaces always requires the introduction of a smoothed process. In fact, in any engineering matter we have to deal with

physical fractals, as dictated by each particular application. In remote sensing radar applications two different parameters establish the scales of interest for the definition of the physical fractal, i.e. of the considered smoothed process. The first is the wavelength λ of the electromagnetic field used to sense the scene: as a matter of fact, objects with dimension lower than a fraction of this wavelength don't contribute significantly to the generation of the backscattered signal. In this sense, we have to introduce a first smoothing on the surface, where the ε of interest has to be set equal to this fraction of λ. However, a second parameter has to be taken into account, i.e. the sensor resolution Δx: in fact, the observed scene is filtered according to the sensor impulse response and scales smaller than the resolution one do not significantly contribute to the formation of the final intensity image. This allows us to conveniently employ the fBm smoothed process presented in the previous section. In particular, if $\Delta x >> \lambda$, as the case for radar remote sensing, we can neglect the first filtering step of our chain and work directly on the following process:

$$z(x;\Delta x) = \int_{-\infty}^{\infty} z(x')\varphi(x-x')dx' \quad , \tag{4.23}$$

where the ε in (4.7) has been set equal to the sensor resolution cell dimension Δx.

Hence, if we assume that the slopes of the observed profile are adequately small we can expand the SPM expression of the backscattering coefficient (the expression given in Chapter 2, adapted to the one-dimensional case) into a Mac Laurin series and, combining (4.1) and (4.23) we can obtain:

$$i(x;\Delta x) \cong a_0 + a_1 p(x;\Delta x) \tag{4.24}$$

wherein, thanks to the results presented in the previous sub-section, we can state that $p(x;\Delta x)$ is the fGn process associated to the imaged fBm profile. Equation (4.24) states that the image inherits the stochastic behavior of the fGn process, i.e. it is Gaussian distributed with $\mu = a_0$ and $\sigma = a_1 s \Delta x^{H-1}$, as can be easily argued combining previously obtained results with Eq. (4.24). It is interesting to note that

the expression in (4.24) allows also the introduction of a two-scale fractal model, based on two different sets of fractal parameters at microscopic and macroscopic scale. As a matter of fact, while $p(x;\Delta x)$ is dependent on the fractal parameters at resolution scale, the constants a_0 and a_1 depend on the fractal parameters of the surface at scales lower than the resolution one, as previously anticipated. A block scheme of the presented imaging process is provided in Fig. 1.

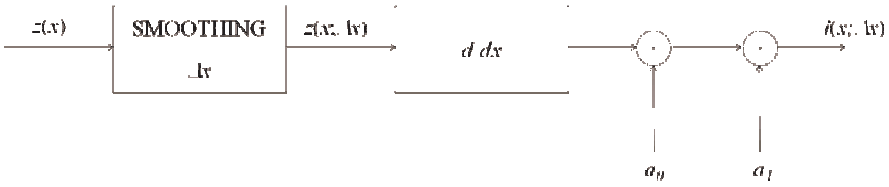

Figure 1 Block diagram of the small slope imaging process.

However, a combined use of the expression in (4.24) with the results regarding the fGn process provides the following behaviors for the structure function V_I and the power density spectrum S_I of the image intensity:

$$V_I(\tau;\Delta x) = a_1^2 V_{z'}(\tau;\Delta x) \tag{4.25}$$

$$S_I(k;\Delta x) = a_1^2 S_{z'}(k;\Delta x) \tag{4.26}$$

The plots relative to (4.25) and (4.26) are shown in Fig. 2 and Fig. 3 respectively, where the behavior is compared with that of the profile of reference.

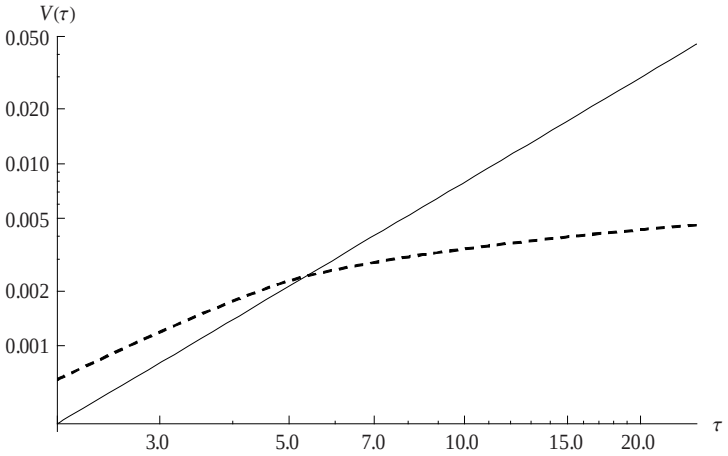

Figure 2 Log-Log variogram of the surface (full line) and of its derivative (dashed line): $H = 0.95$; $s = 0.01$ m$^{(1-H)}$; $\Delta x = 5$ m, $a_1 = 10$.

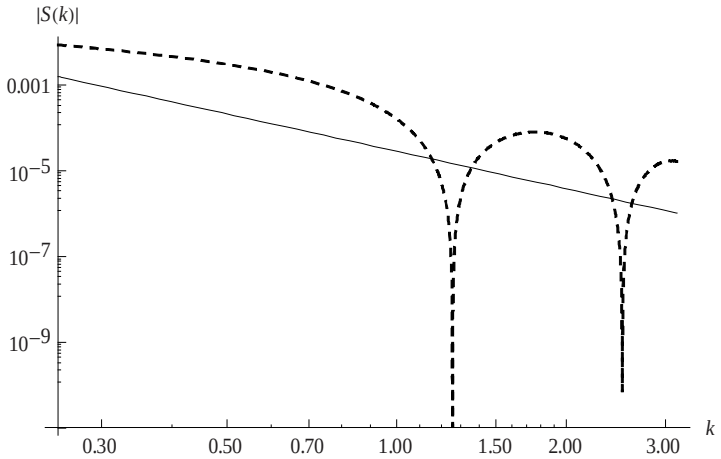

Figure 3 Log-Log plot of the spectra of the surface (full line) and of its derivative (dashed line): $H = 0.95$; $s = 0.01$ m$^{(1-H)}$; $\Delta x = 5$ m, $a_1 = 10$.

The result shown in (4.26) is analogous to the one obtained by Pentland only in the asymptotic limit in which S_I is given by Eq. (4.22). In fact, the formal use of the surface derivatives allows Pentland working with $\varepsilon = 0$ rigorously, i.e. always in a regime of validity of the abovementioned asymptotic expressions.

A common misinterpretation of Pentland results is that the fractal dimension of the image is equal to the fractal dimension of the imaged

surface. Looking at (4.25) and (4.26), we can state that this is incorrect and that, at most (asymptotically), the spectral behavior would suggest a fractal dimension of the image $D_I = D_T - 1$, where D_T is the fractal dimension relevant to the observed scene. As already mentioned, this would be in agreement with the observation made by Voss [15] on the fractal dimension of the derivative process of an fBm, suggesting that the Hurst parameter, upon differentiation, is decreased by one. Nevertheless, as we already argued above, the possibility of defining a fractal dimension for such a process is questionable and we can state that the image of a fractal surface is not a fractal.

An important peculiarity of microwave images, and, more in general, of every coherent imaging system, is the speckle effect, due to the constructive and destructive interferences between individual plane waves in each resolution cell, which also claims for a specific characterization in the fractal case [10]. Anyway, at the moment we focus on the ideal case of an infinite number of looks: in this limit the effects of the speckle are completely discarded. However, removing this very tight assumption is an important step toward a complete modeling of the microwave imaging process of fractal profiles.

Some considerations on the retrieval of the fractal parameters of the observed profile from the image are now in order. In fact, this image is not a fractal but a relation between the fractal parameters of the profile and the obtained image does exist. As shown in Chapter 2 and 3, the fractal parameters estimation techniques for an fBm are based on linear regressions on log – log plots of the variogram or of the power density spectrum. This simple technique cannot be directly used on the image. In particular, it is evident that if we use the general expressions obtained from (4.25) and (4.26) a linear regression in the log – log plane is no longer possible. Anyway, in most cases, use can be made of the asymptotic expressions obtained from (4.16) and (4.22): in this case for the structure function things keep not working perfectly, but, conversely, for the power density spectrum a power-law behavior can be assumed in the band of interest and the fractal parameters can be recovered via the standard log – log linear regression procedure.

However, the interesting thing is that the possibility to use the asymptotic expression of the spectrum comes out to be dependent on sensor resolution. In particular, for new generation high resolution

sensors also the hypothesis we made at the beginning of this section, i.e. $\Delta x >> \lambda$, could be not verified: this means problems can begin to rise when we increase sensor resolution. By the way, we note that high resolution sensors, reducing the range of spatial frequencies of the surface contributing to speckle formation, can determine a change in noise statistics on intensity images, as we have seen in Chapter 1. Anyway, an exhaustive study of these phenomena is widely beyond the scope of this work.

4.1.2.3 The numerical framework

In the present section a numerical framework, based on effective direct geometric and electromagnetic models, is used to analyze the imaging process of a one-dimensional fractal profile. This analysis allows the study of the imaging of a generic profile, without the need of assuming any particular hypothesis on its slope. Note that this elaboration chain is widely based on the models and tools presented in the previous chapter.

The first step is the generation of the fractal fBm profile. This is achieved using the Weierstrass-Mandelbrot (WM) function [16]: indeed, under some hypothesis, the WM effectively approximates an fBm profile, as we have seen in Chapter 2. Furthermore, the WM is a predictable random function and this greatly simplifies the control of the behavior of the profile, acting on its random parameters. The inputs for this first block are the fractal parameters (s and H) of the profile.

When the profile is synthesized, we evaluate the backscattered signal via the SPM fractal scattering model. As previously mentioned, the geometrical model used in this section is based on the assumption that the observed profile shows the same fractal parameters at all the scales of interest: in particular, at scales greater and lower of the resolution one. Note that, if this was not the case, the parameters H and s used in (4.25) and (4.26) would refer to the fractal parameters of the profiles at scales greater than the resolution one. Conversely, for the evaluation of the backscattered signal via the SPM model the fractal parameters to be used are those relevant to the microscopic scale, as argued in the previous chapter. The inputs for this block are given in term of sensor resolution, sensor height, semi-aperture angle

and, finally, look angle: through these parameters the software is able to evaluate the extension of the scene and the number of samples.

The final step is the estimation of the power density spectra of the original profile and of the computed backscattered signal to compare them with the analytical results presented in the previous sections. Note that the evaluation of these power law spectra is not a trivial issue, because they are subject to extreme leakage and high variance problems. Among the techniques used to effectively retrieve these spectra, we chose the Capon filtering, which is widely assumed to be the optimum one (see Ref. [17] for details). Nevertheless, the high and low frequency regions of the estimated spectra cannot be evaluated with adequate accuracy. The main results obtained are presented in the following sub-section.

4.1.2.4 The obtained results

The parameters used in all the simulations presented in the following are reported in Table I. Note that in all the simulation a VV polarization has been assumed, and for the used values of the parameters no significant variation in the results has been observed changing the polarization. The first elaboration is relevant to a case in which the small slope hypothesis can be widely assumed to be valid. In fact, looking at the obtained results shown in Fig. 4, the good fit between the estimated spectra and the theoretical ones is evident. Note that in all the figures, unless the contrary is not explicitly stated, the various plots are in a log – log scale and are superimposed to simplify the comparison of the spectral slopes.

In Fig. 5, 6 and 7 simulations in which the small slope hypothesis is no longer rigorously satisfied are instead presented: in fact, a certain mismatch between the experimental and theoretical results begins to appear. This result is obtained increasing the roughness of the imaged profile, thus increasing its mean slope. However, it’s important to note that in the fractal case speaking simply of roughness is not enough: also the scale of interest should be specified. This is the reason why the validity limits of the small slope hypothesis for the SPM scattering model need to be deeply investigated in a dedicated work.

Table 1 List of the parameters used in the simulations and summary of results.

	Fig. 4	Fig. 5	Fig. 6	Fig. 7	Fig. 8	Fig. 9
Frequency [GHz]	1	1	1	1	1	1
Resolution [m]	5	5	5	5	20	1
Sensor height [km]	10	10	10	10	40	2
Semi-aperture angle [°]	10	10	10	10	10	10
Look angle [°]	10	10	10	10	10	10
H	0.95	0.55	0.95	0.55	0.95	0.95
s [m^{1-H}]	0.01	0.01	1	1	0.01	0.01
Expected spectral slope	-0.900	-0.100	-0.900	-0.100	-0.900	-0.900
Retrieved spectral slope	-0.922	-0.246	-0.775	-0.239	-0.925	-0.934
Squared distance	0.0092	0.0992	0.0082	-	-	-

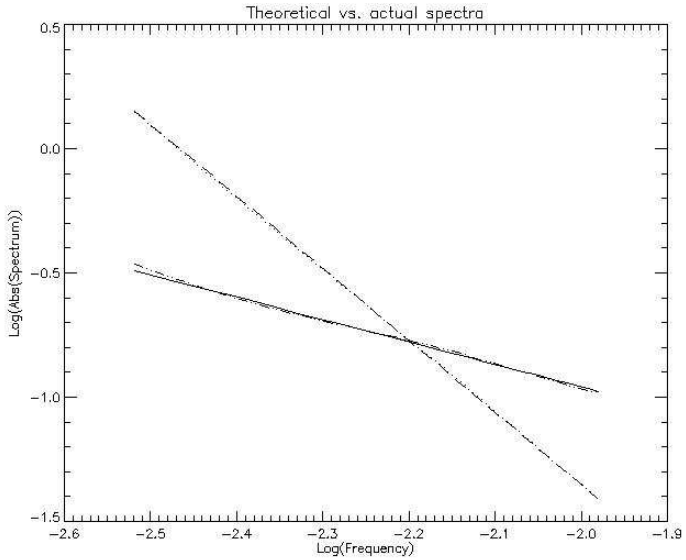

Figure 4 Theoretical spectra of the surface (long dashed) and of the image (full line) versus the estimated ones (dotted and dash dot dot, respectively).

Obviously, the main interest for applications is in retrieving the spectral slope of the surface working on its microwave image, hence to provide quantitative indicators of the agreement between theoretical and experimental results the slopes of the obtained spectra is estimated via a simple linear regression algorithm and reported in Table I. Furthermore, in Table I the square distance between the experimental points and the fitted curve is provided: this can be seen as a quantitative measure of the degree of linearity of the retrieved spectra. As can easily be noted, as the slope estimate begins to get worse the distance begins to increase: this means that the spectrum begins to lose its log – log linear behavior. The interesting thing is that this seems to be related more to a variation in the *Hurst parameter* than to a variation in *s*. This is another reason claiming for a deeper investigation of the validity limits of the small slope hypothesis for the SPM scattering model.

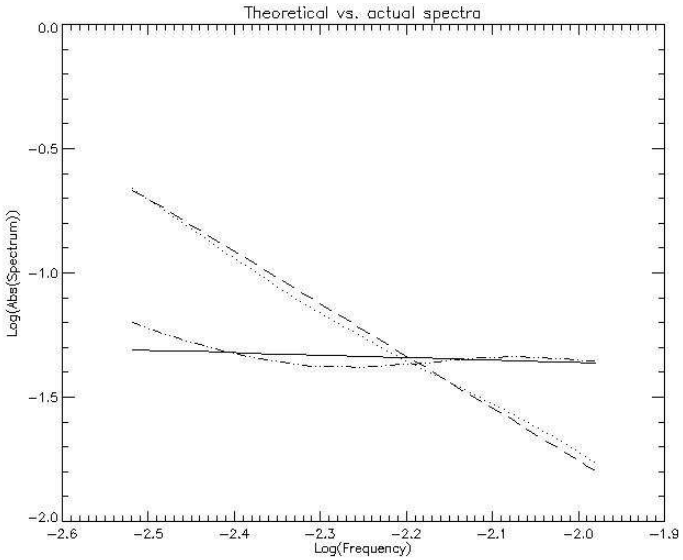

Figure 5 Theoretical spectra of the surface (long dashed) and of the image (full line) vs. estimated ones (dotted and dash dot dot, respectively).

In Fig. 8 and 9 we focus on the role of resolution. In fact, no significant difference can be noted in the goodness of fit of the curves as the resolution varies, apart from a very little worsening of the goodness of fit in the 20 meters resolution case. The reason is that the

variation in resolution is too small to determine a failure in the small slope hypothesis assumption. However, taking into account resolution much coarser than the one proposed here (20 m) is, at this moment, of scarce practical interest. Finally, in Fig. 10 we present a combination of Fig. 4, 8 and 9 which clearly shows how a variation in sensor resolution allows an investigation of the profile spectral and spatial properties over an increased range of scales, and how each obtained plot is consistent to the others. However, we analyzed also the case of a variation in resolution for the worst case scenario (H = 0.55 and s = 1 $m^{0.45}$), obtaining results quite similar to the one of the 5 meters resolution case.

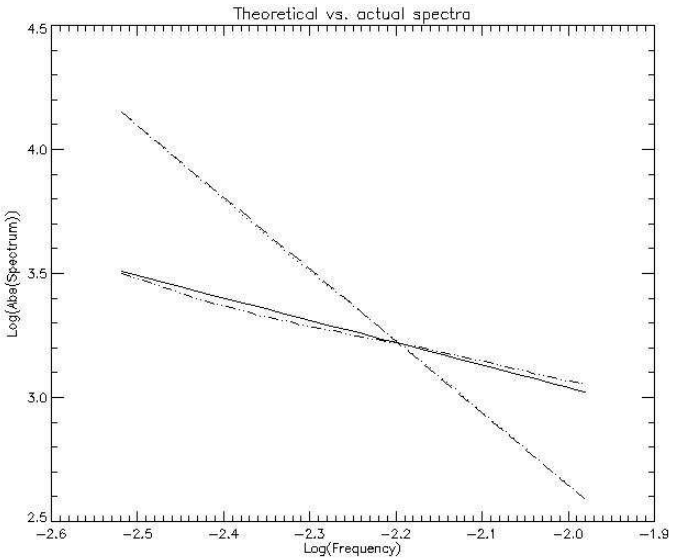

Figure 6 Theoretical spectra of the surface (long dashed) and of the image (full line) vs. estimated ones (dotted and dash dot dot, respectively).

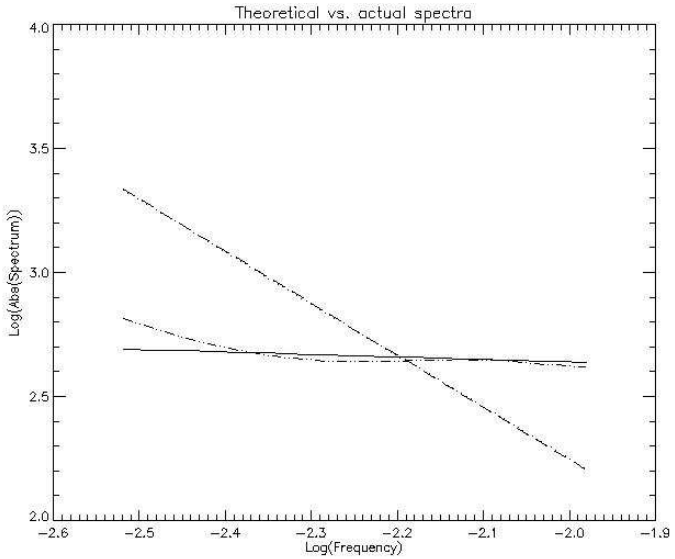

Figure 7 Theoretical spectra of the surface (long dashed) and of the image (full line) vs. estimated ones (dotted and dash dot dot, respectively).

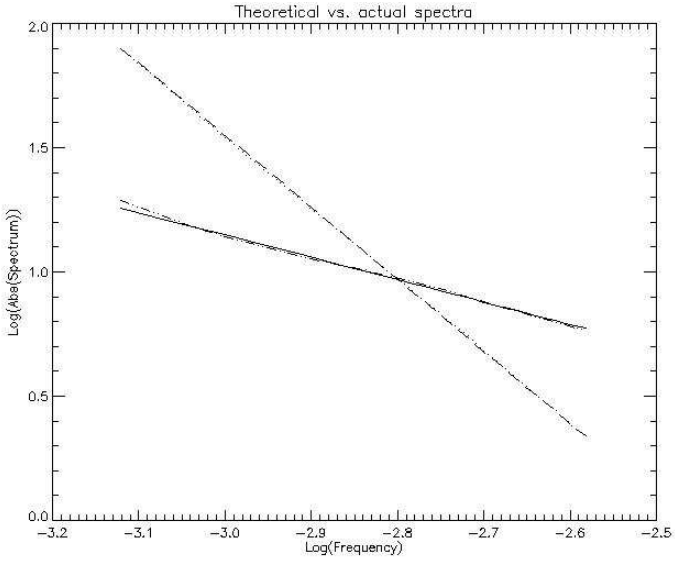

Figure 8 Theoretical spectra of the surface (long dashed) and of the image (full line) vs. estimated ones (dotted and dash dot dot, respectively).

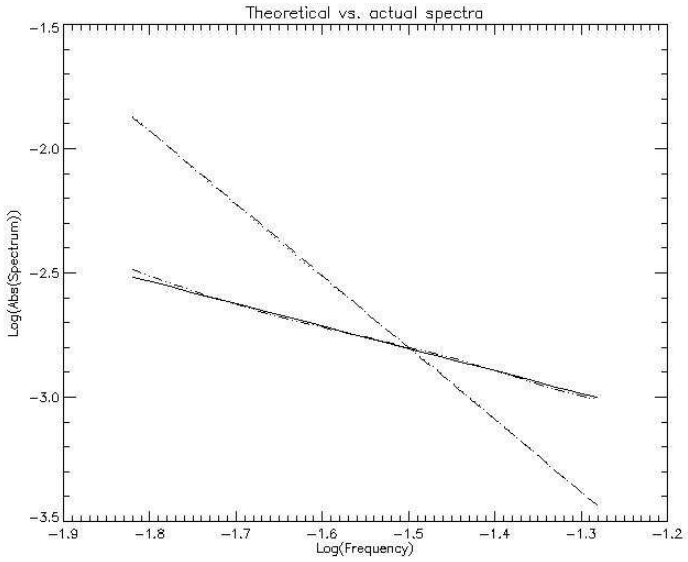

Figure 9 Theoretical spectra of the surface (long dashed) and of the image (full line) vs. estimated ones (dotted and dash dot dot, respectively).

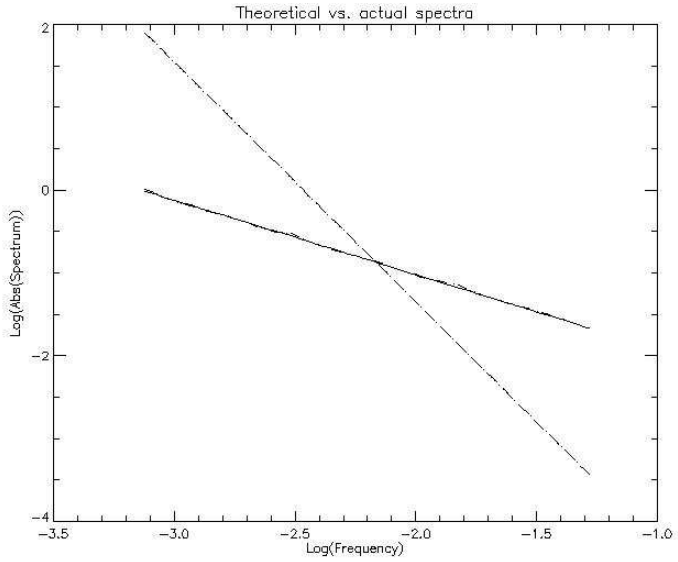

Figure 10 Theoretical spectra of the surface (long dashed) and of the image (full line) vs. estimated ones (dotted and dash dot dot, respectively). This figure is obtained combining Fig. 4, 8 and 9.

The key result we can draw from this numerical study is that microwave images of fractals profiles are not fractal, both if the small slope regime can be assumed (as we have seen in the previous section) or not. In fact, in the latter case the spectral behavior of the backscattered signal is no longer a power law one. However, a relation between the fractal parameters of the profile and the texture of the obtained image exists and shall be used in the definition of appropriate inversion techniques.

From our analysis of this process we drew two main conclusions relevant to the images of fractal profiles, in case a small slope regime can be assumed:

- they are stationary Gaussian self-affine processes, but not fractal processes, in the sense that we cannot define a Hausdorff-Besicovitch fractional dimension for this class of signals;
- asymptotically, for sufficiently low frequencies, their spectrum has a power law behavior.

Finally, the proposed approach leads to the conclusion that the radar image of a fractal profile cannot be assumed to be fractal in any case. However, a relation between the fractal parameters of the original profile and the obtained image exists and in this work a possible expression of this relation has been provided.

4.2 The two-dimensional problem: preliminary results

In this section the first results obtained for the two-dimensional imaging problem are presented. We show how a closed form expression for the spectrum of the two-dimensional image of a fractal surface can be obtained. This first results are not fully two-dimensional ones, in fact the spectrum is computed only for one-dimensional cuts in range and azimuth directions. Furthermore, the case of the range cut is not discussed here in detail, due to the fact that it leads to an expression perfectly equal to that obtained in the one-dimensional case.

First of all we need to investigate potential differences in the role of the two partial derivatives of the surface in the contest of the imaging process. Let us try to develop the SPM scattering function in McLaurin series to the first order. We have to find the relation between the local incidence angle and the partial derivatives of the surface. It is easy to verify that the required relation is:

$$\cos\vartheta = \frac{p\sin\theta_0 + \cos\theta_0}{\sqrt{p^2+q^2+1}} \tag{4.27}$$

where ϑ is the local incidence angle, θ_0 is the look angle of the sensor and p and q are the partial derivatives of the surface in range and azimuth direction, respectively. Accordingly,

$$\sin\vartheta = \sqrt{1-\cos^2\vartheta} = \frac{\sqrt{(\sin\theta_0 - p\cos\theta_0)^2 + q^2}}{\sqrt{p^2+q^2+1}} \tag{4.28}$$

Substituting (4.27) and (4.28) into the expression of the RCS computed with the SPM and discarding the polarization factor β_{pq} (which is practically constant for our purposes) we obtain:

$$I(p,q) = A_0\left(\frac{(\cos\theta_0 + psen\theta_0)^2}{p^2+q^2+1}\right)^2\left(\frac{(sen\theta_0 - p\cos\theta_0)^2 + q^2}{p^2+q^2+1}\right)^{-(1+H)} \tag{4.29}$$

Expanding Eq. (4.29) in a McLaurin series to the first order for small values of p and q we obtain an important result. In fact, it comes out that at the first order the image is related linearly only to the partial derivative in the range direction p. This is due to the particular acquisition geometry of the SAR sensor, which clearly presents a preference range direction. This allows us to focus only on the expression of the range derivative of the surface.

To obtain analytical solutions for the two-dimensional problem we have to deal with the following regularized version of the surface:

$$z_{\varphi}(x,y)=\iint z(x',y')\varphi(x-x',y-y')dx'dy' \tag{4.30}$$

with

$$\varphi(x,y)=\begin{cases}\dfrac{1}{\varepsilon\eta} & \text{if } (x,y)\in[0,\varepsilon]\times[0,\eta]\\ 0 & \text{otherwise}\end{cases} \tag{4.31}$$

with $\varepsilon>0,\ \eta>0$.

The partial derivative in the range direction can be computed as follows:

$$\begin{aligned}\frac{\partial z_{\varphi}}{\partial x}&=-\iint z(x',y')[\delta(x-x')-\delta(x+\varepsilon-x')](\varepsilon\eta)^{-1}dx'dy'=\\&=(\varepsilon\eta)^{-1}\int_{y-\eta}^{y}[z(x+\varepsilon,y')-z(x,y')]dy'\end{aligned} \tag{4.32}$$

with simple mathematical manipulations we obtain the following expression for the auto-correlation function of the azimuth cuts of the partial derivative process:

$$R_p(\tau_y;\varepsilon,\eta)=s^2\varepsilon^{-2}\left[\left|\tau_y^2+\varepsilon^2\right|^H-\left|\tau_y\right|^{2H}\right] \tag{4.33}$$

where τ_y is a distance in the range direction only.

For the same reasons exposed in the previous section, we can compute the spectra as the FT of the auto-correlation (note that generalized FTs have to be introduced), obtaining:

$$W_p(k_y;\varepsilon)=s^2\varepsilon^{-2}\left[\frac{2^{\left(\frac{3}{2}+H\right)}\sqrt{\pi}\varepsilon^{\left(\frac{1}{2}+H\right)}\left|k_y\right|^{-\left(\frac{1}{2}+H\right)}K_{\frac{1}{2}+H}\left(\left|k_y\right|\varepsilon\right)}{\Gamma(-H)}+2\left|k_y\right|^{-\left(\frac{1}{2}+H\right)}\Gamma(1+2H)\sin(\pi H)\right] \tag{4.34}$$

Accordingly, the power density spectrum of an azimuth cut of the image will be, using the previously introduced formalism:

$$W_I(k_y;\Delta x) = a_1^2 s^2 \Delta x^{-2} \left[\frac{2^{\left(\frac{3}{2}+H\right)} \sqrt{\pi} \Delta x^{\left(\frac{1}{2}+H\right)} \left|k_y\right|^{-\left(\frac{1}{2}+H\right)} K_{\frac{1}{2}+H}\left(\left|k_y\right|\Delta x\right)}{\Gamma(-H)} + 2\left|k_y\right|^{-\left(\frac{1}{2}+H\right)} \Gamma(1+2H)\sin(\pi H) \right] \tag{4.35}$$

Conversely, as we mentioned before, as for the range cuts their behavior is equal to the case of one-dimensional profile.

A numerical framework for the study of the two-dimensional case has been developed, by simple extension from the one-dimensional case. The results are analogous to those obtained for the one-dimensional case and a good agreement is found between the actual and the theoretical power density spectrum of both range and azimuth cuts, as shown in Fig. 11 and 12, respectively.

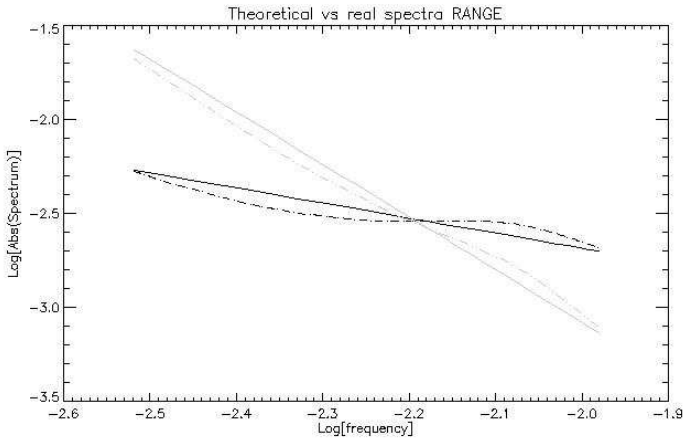

Figure 11 Theoretical spectra of the surface (long dashed) and of the image (full line) vs. estimated ones (dotted and dash dot dot, respectively).

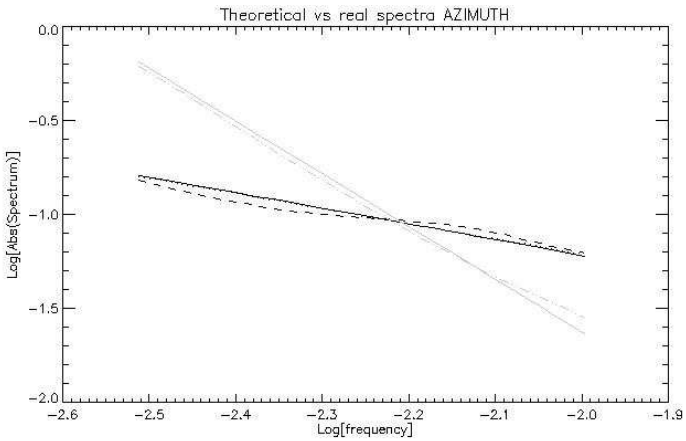

Figure 12 Theoretical spectra of the surface (long dashed) and of the image (full line) vs. estimated ones (dotted and dash dot dot, respectively).

Further developments of the proposed approach should be focused on the fully two-dimensional problem and, more in general, to the introduction in the model of geometrical distortions and speckle noise.

References

[1] J. M. Lopez-Sanchez, J. D. Ballester-Berman, Y. Marquez-Moreno, "Model limitations and parameters-estimation methods for agricultural applications of polarimetric SAR interferometry", *IEEE Trans. Geosci. Remote Sens.*, vol. 45, no.11, pp. 3481-3493, Nov. 2007.

[2] C. Arai, N. Matsuda, M. Shikada, "An application of remote sensing and REAL TIME GIS to digital map for local government", in *Proc. IGARSS*, 2003, pp. 4552-4554.

[3] S. Voigt, T. Kemper, T. Riedlinger, R. Kiefl, K. Scholte, H. Mehl, "Satellite image analysis for disaster and crisis-management support", *IEEE Trans. Geosci. Remote Sens.*, vol. 45, no. 6, pp. 1520-1528, June 2007.

[4] B.B. Mandelbrot, *The Fractal Geometry of Nature*. New York: Freeman, 1983.

[5] K. Falconer, *Fractal Geometry*. Chichester, U.K.: Wiley, 1989.

[6] J.S. Feder, *Fractals*. New York: Plenum, 1988.

[7] A. Pentland, “Fractal-based description of natural scene”, *IEEE Trans. Pattern Anal. Mach. Intell.*, vol. PAMI-6, no.6, pp. 661-674, Nov. 1984.

[8] P. Kube and A. Pentland, “On the imaging of fractal surfaces”, *IEEE Trans. Pattern Anal. Mach. Intell.*, vol. 10, no. 5, pp.704-707, Sep. 1988.

[9] G. Franceschetti, D. Riccio, *Scattering, Natural Surfaces and Fractals*. Academic Press, Burlington (MA), USA, 2007.

[10] G. Franceschetti, M. Migliaccio, D. Riccio, "An electromagnetic fractal-based model for the study of the fading", *Radio Sci.*, vol. 31, no. 6, pp. 1749-1759, Nov./Dec.1996.

[11] G. Korvin, “Is the optical image of a non-lambertian fractal surface fractal?”, *IEEE Geosci. Remote Sens. Lett.*, vol. 2, no. 4, pp. 380-383, Oct. 2005.

[12] P. Addesso, S. Marano, R. Restaino, M. Tesauro, “Correlation properties of signals backscattered from fractal profiles”, *IEEE Trans. Geosci. Remote Sens.*, vol. 45, no. 9, pp. 2859-2868, Sep. 2007.

[13] B. B. Mandelbrot and J. W. Van Ness, “Fractional Brownian motions, fractional noises and applications”, *SIAM Rev.*, vol. 10, no.4, pp.422-437, 1968.

[14] I.M. Gelfand e G.E. Shilov, *Generalized Functions Vol. 1*, Academic Press, Burlington (MA), USA, 1964.

[15] R. F. Voss, “Random Fractal Forgeries”, in *Fundamental Algorithms for Computer Graphics*, R. A. Earnshaw, Ed. New York: Springer-Verlag, 1985, pp. 805-835.

[16] M.V. Berry and Z.V. Lewis ,"On the Weierstrass-Mandelbrot fractal function", *Proc. R. Soc. Lond. A, Math. Phys. Sci.*, Apr. 1980, vol. 370, pp.459-484.

[17] T. Austin, A. W. England, G. H. Wakefield, “Special problems in the estimation of power-law spectra as applied to topographical modeling”, *IEEE Trans. Geosci. Remote Sens.*, vol. 32, no. 4, pp. 928-939, July 1994.

Summary and conclusions

In this thesis the extraction of value-added information from SAR images has been discussed. In particular, the need for adequate models accounting for the transmission of information from the observed surface to its radar image has been highlighted.

The original contributions presented in this work range from the development of SAR simulation tools to the analysis of actual high resolution data, passing through the whole modeling of the imaging process of fractal profiles.

Particularly, in Chapter 1 a preliminary analysis of the new high resolution TerraSAR-X data is presented, showing the need for new models for the characterization of high resolution SAR images.

As for the simulation tools, a whole simulation and analysis chain has been developed and tested. The main feature of the presented chain is the possibility to provide an effective test bed for the development of automatic analysis techniques. A novel change detection technique based on fractal concepts is also presented and tested. Finally, new simulation facilities for the case of ocean scenes covered with oil slicks have been developed, allowing the use of fractal geometry for the synthesis and subsequent discrimination of natural and man-made slicks on the sea surface.

Finally, the main original contribution of this thesis work is detailed in Chapter 4, where the characteristics of images relevant to a fractal profile are investigated.

In our study we follow a twofold approach: on one side, we develop a rigorous analytical formulation for the problem assuming a particular class of small slope profiles; on the other side, we present an experimental setup able to deal with the more general case. As for the analytical approach, we show that the signal backscattered from a fractal profile modeled as an fBm stochastic process is strictly related to the associated fractional Gaussian noise (fGn) process when a small slope regime for the observed profile holds: in this case we are able to compute in closed form the structure function and the spectrum of the signal. Our results are obtained introducing an fBm smoothed process,

which is justified by the low-pass filtering introduced by the sensor impulse response function.

The experimental framework is based on sound direct models allowing the synthesis of the profile, the evaluation of the backscattered signal via fractal scattering models and the estimation of the power density spectra of interest. Note that this is the only fully fractal approach found in the open literature on this subject, i.e. with a coherent choice of the geometric and electromagnetic models.

This twofold approach leads to the conclusion that the radar image of a fractal profile cannot be assumed to be fractal in any case. However, a relation between the fractal parameters of the original profile and the obtained image exists. Thus, further developments of the models provided in this thesis work are of key importance for the progress of future information extraction techniques.